Digital process design to define and deliver pharmaceutical particle attributes

Stephanie J. Urwin[a], Magdalene W.S. Chong[a,b,1], Wei Li[c,1],
John McGinty[a,d,1], Bhavik Mehta[a,e,1], Sara Ottoboni[a,d,1],
Momina Pathan[a,1], Elke Prasad[a,1], Murray Robertson[a,1],
Mark McGowan[a], Mais al-Attili[d], Ekaterina Gramadnikova[a],
Mariam Siddique[a], Ian Houson[a], Helen Feilden[a], Brahim Benyahia[c],
Cameron J. Brown[a,f], Gavin W. Halbert[a,f], Blair Johnston[a,f],
Alison Nordon[a,b], Chris J. Price[a,d], Chris D. Reilly[c], Jan Sefcik[a,d],
Alastair J. Florence[a,*]

[a] EPSRC Future Manufacturing Hub in Continuous Manufacturing and Advanced Crystallisation, University of Strathclyde, Glasgow G1 1RD, UK
[b] WestCHEM, Department of Pure and Applied Chemistry, and Centre for Process Analytics and Control Technology (CPACT), University of Strathclyde, Glasgow G1 1XL, UK
[c] Future Continuous Manufacturing and Advanced Crystallisation, Research Hub at the Department of Chemical Engineering, Loughborough University, Loughborough LE11 3TU, UK
[d] Department of Chemical and Process Engineering, University of Strathclyde, Glasgow G1 1XJ, UK
[e] Siemens Process Systems Engineering Ltd, London W6 7HA, UK
[f] Strathclyde Institute of Pharmacy & Biomedical Science, University of Strathclyde, Glasgow G4 0RE, UK

ARTICLE INFO

ABSTRACT

A digital-first approach to produce quality particles of an active pharmaceutical ingredient across crystallisation, washing and drying is presented, minimising material requirements and experimental burden during development. To demonstrate current predictive modelling capabilities, the production of two particle sizes (D_{90} = 42 and 120 μm) via crystallisation was targeted to deliver a predicted, measurable difference in in vitro dissolution performance. A parameterised population balance model considering primary nucleation, secondary nucleation and crystal growth was used to select the modes of production for the different particle size batches. Solubility prediction aided solvent selection steps which also considered manufacturability and safety selection criteria. A wet milling model was parameterised and used to successfully produce a 90 g product batch with a particle size D_{90} of 49.3 μm, which was then used as the seeds for cooling crystallisation. A rigorous approach to minimising physical phenomena observed experimentally was implemented, and successfully predicted the required conditions to produce material satisfying the particle size design objective of D_{90} of 120 μm in a seeded cooling crystallisation using a 5-stage MSMPR cascade. Product material was isolated using the filtration and washing processes designed, producing 71.2 g of agglomerated product with a primary particle D_{90} of 128 μm. Based on experimental observations, the population balance model was reparametrised to increase accuracy by inclusion of an agglomeration term for the continuous cooling crystallisation. The dissolution performance for the two crystallised products is also demonstrated, and after 45 min

104.0 mg of the D_{90} of 49.3 μm material had dissolved, compared with 90.5 mg of the agglomerated material with D_{90} of 128 μm. Overall, 1513 g of the model compound was used to develop and demonstrate two laboratory scale manufacturing processes with specific particle size targets. This work highlights the challenges associated with a digital-first approach and limitations in current first-principles models are discussed that include dealing *ab initio* with encrustation, fouling or factors that affect dissolution other than particle size.

Nomenclature

List of abbreviations and acronyms

API	Active pharmaceutical ingredient.
ATR	Attenuated total reflectance.
BCS	Biopharmaceutics classification system.
CBA	2-Chlorobenzoic acid.
CMA	Critical material attribute.
CPME	Cyclopentyl methyl ether.
CPP	Critical process parameter.
CQA	Critical quality attribute.
DCS	Developability classification system.
DMA	*N,N*-Dimethylacetamide.
DMF	*N,N*-Dimethylformamide.
DMSO	Dimethylsulfoxide.
DNC	Direct nucleation control.
DoE	Design of experiments.
EMA	European Medicines Agency.
FBRM	Focused beam reflectance measurement.
FDA	Food and Drug Administration.
gFP	gPROMS FormulatedProducts®.
GI	Gastrointestinal.
GSA	Global sensitivity analysis.
HPLC	High performance liquid chromatography.
ICH	International Council of Harmonisation.
2-MeTHF	2-Methyltetrahydrofuran.
MFA	Mefenamic acid.
MSMPR	Mixed-suspension mixed product removal.
MSZW	Metastable zone width.
PAT	Process analytical technology.
PBE	Population balance equation.
PBM	Population balance model.
PLS	Partial least squares.
PSD	Particle size distribution.
QbD	Quality by design.
RMSE	Root mean square error.
rpm	Revolutions per minute.
RSD	Relative standard deviation.
UV	Ultraviolet.

Definition of terms

A	Filter area (m^2).
A_g	Agglomeration efficiency (-).
A_{50}	Bridging strength parameter (-).
b_1	Primary nucleation supersaturation power (-).
b_2	Secondary nucleation supersaturation power (-).
C^*	Saturation concentration at given temperature (-).
C_0	Wet milling intercept parameter (s^{-1}).
C_{Cryst}	Solute concentration (-).
C_{Iso}	Dry cake mass per unit volume of filtrate ($kg\ m^{-3}$).
C_{WM}	Shear rate (s^{-1}).
c_j	Concentration of species j in the filtrate (-).
$c_{j,i}$	Initial concentration of species j in the filtrate (-).
$c_{j,w}$	Concentration of species j in the inlet wash stream (-).
D_L	Axial dispersion coefficient ($m^2\ s^{-1}$).
d_e	Equivalent particle diameter (m).
f_1	Difference factor (-).
f_2	Similarity factor (-).
G	Growth rate ($m\ s^{-1}$).
G_d	Dissolution rate ($m\ s^{-1}$).
g	Supersaturation power (-).
g_d	De-supersaturation power (-).
J_1	Primary nucleation rate ($m^{-3}\ s^{-1}$).
J_2	Secondary nucleation rate ($m^{-3}\ s^{-1}$).
k_{Iso}	Absolute permeability (m^2).
k_{b1}	Primary nucleation rate constant ($m^{-3}\ s^{-1}$).
k_{b2}	Secondary nucleation rate constant ($m^{-3}\ s^{-1}$).
k_g	Growth rate constant ($m\ s^{-1}$).
k_{gd}	Growth rate constant (-).
k_v	Volume shape factor (-).
L	Cake thickness (m).
L_{min}	Particle size leading to attrition in crystal and impellor collisions (m).
N_{cap}	Number of capillary (-).
N_P	Impellor power number (-).
N_Q	Impellor flow number (-).
$N_{\gamma-\delta}$	Number of rotor-stator rows in wet milling (-).
n	Energy input order ($m^{-3}\ m^{-1}$).
P	Pressure ($kg\ m^{-1}\ s^{-2}$).
P_b	Threshold pressure value (Pa).
Δp	Imposed pressure drop for the gas flow (Pa).
R_m	Filter medium resistance (m^{-1}).
S	Breakage rate (s^{-1}).
S_{Cake}	Cake saturation (-).
Sc_M	Constant rate of breakage at critical size (s^{-1}).
S_{Cryst}	Absolute supersaturation (-).
S_R	Reduced saturation (-).
S_{WM}	Wet milling breakage rate ($μm\ s^{-1}$).
S_∞	Irreducible saturation (-).
T	Temperature (K).
T_f	Final process temperature (°C).
T_i	MSMPR stage temperature (°C).
t	Time (min).
u_s	Superficial velocity of wash ($m\ s^{-1}$).
V	Volume (mL).
V_{Iso}	Filtrate volume removed (m^3).
X_{But}	Mass fraction (concentration) of 2-butanol (-).
X_{CBA}	Mass fraction (concentration) of 2-chlorobenzoic acid (-).

X_{Dig}	Mass fraction (concentration) of diglyme (-).
X_{Hept}	Mass fraction (concentration) of n-heptane (-).
X_{MFA}	Mass fraction (concentration) of mefenamic acid (-).
x_{sv}	Particle volume equivalent diameter (m).
y	Breaking particle size (μm).
α_{av}	Media resistance (m kg^{-1}).
α'	Wet milling kernel parameter (-).
β'	Wet milling kernel parameter (-).
γ_{PBM}	Wet milling kernel parameter (-).
γ_{WM}	Wet milling kernel parameter (-).
δ_i	Horizontal gap between rotor and stator (m).
ε_{av}	Cake porosity average (-).
ε_{Iso}	Cake porosity (-).
ε_{PBM}	Energy dissipation rate (m^2 s^{-3}).
θ	Set of model parameters to be estimated (-).
μ_{Iso}	Filtrate viscosity (kg m^{-1} s^{-1}).
μ_{PBM}	Chemical potential (J kg^{-1}).
ρ_c	Slurry density (kg m^{-3}).
ρ_l	Filtrate density (kg m^{-3}).
ρ_s	Solid density (kg m^{-3}).
σ	Interfacial tension of filtrate (N m^{-1}).
τ	Residence time (min).
υ	Product particle volume (m^3).
$\upsilon_{ts,t}$	Wet milling rotor/impellor tip speed (m s^{-1}).
ϕ	Wet milling kernel parameter (-).
ω	Breaking particle volume (m^3).
$\omega_{critical}$	Critical volume preventing particle from further breakage (m^3).

1. Introduction

Whilst predictive modelling is widely used in some areas of chemical and process engineering, the application of "digital-first" approaches in pharmaceutical manufacturing has been limited (Destro and Barolo, 2022). To ensure patient safety, product specifications for medicines are often narrower than in other types of manufacturing. With strong regulatory oversight and high failure rates during clinical trials,(Suresh and Basu, 2008) the challenge to develop detailed, validated models can be significant. It is essential that the models incorporated within a pharmaceutical digital twin are sufficiently accurate to usefully capture the multiphase, multiphysics and/or multi-scale phenomena that describe the complex relationships between different process parameters and materials/product attributes. This ensures the continued development of safe, effective, quality pharmaceuticals.

We define a digital-first approach as using *in silico* modelling to inform and guide process design, where minimal initial experimentation is undertaken to achieve model parameterisation and a new process can be designed digitally to target specific product attributes. This deviates from the traditional experience-driven approach used in many areas of pharmaceutical manufacturing,(Suresh and Basu, 2008) whereby process design may be based on previous iterative successful processes or through one-parameter-at-a-time approaches. Process models are potentially used retrospectively for streamlining and optimisation. Whole-process models for plant-wide optimisation after development have been reported demonstrating the benefits of end-to-end

models and the application of global sensitivity analysis (GSA) to identify critical quality attributes (CQAs) and critical process parameters (CPPs) (Mascia et al., 2013; Maloney et al., 2020; Liu and Benyahia, 2021; Campbell et al., 2022). One significant evolution of pharmaceutical process development has been the implementation of the quality by design (QbD) framework (ICH, 2008). With a focus on process understanding to embed quality throughout manufacture rather than relying on end-product testing, implementing a QbD strategy naturally results in the application of mathematical models to demonstrate process understanding and control (Chatterjee et al., 2017). Thus, a digital-first approach complements established QbD strategies (Yu et al., 2014). Indeed, the International Council for Harmonisation (ICH) have published guidelines on model implementation for QbD (ICH, 2009). Elements of QbD are frequently used within pharmaceutical research,(Cook et al., 2014) but only around one third of regulatory marketing authorisation applications to the European Medicines Agency (EMA) between 2014 and 2019 used this framework, (ter Horst et al., 2021) illustrating the relatively slow pace of regulatory change within the industry.

There are significant benefits of using a digital-first approach. By removing time- and resource-intensive empirical experimentation, digital design promises a decrease in development time, costs and resources, and will result in a more robust manufacturing process with flexibility within the modelled design space (Suresh and Basu, 2008). Further, incorporation of scale- or hydrodynamic-dependent processes will allow for faster scale-up with more reproducible product quality (Johnson et al., 2021). In empirical process-design, sub-optimal processes are a typical consequence of the time pressure involved in clinical development (Suresh and Basu, 2008). The recent rapid manufacture of Covid-19 vaccines highlights the importance of integrated, rapid process development (van de Berg et al., 2021; Johnson & Johnson Statement on U.S. COVID-19, 2023) and this crisis response provides a new benchmark for the achievable pace of medicines development going forward.

Both the EMA and Food and Drug Administration (FDA) have advocated for increased digitalisation, (Frias et al., 2021; European Medicines Agency Approach to Facilitating Innovative Manufacturing Approaches, 2023; Innovate UK KTN in collaboration with the Advanced Manufacturing Research Centre, 2022) fully incorporating digital tools into regulatory methods. However the perceived difficulties of introducing a new approach under time and cost pressure often lead to risk adverse process developers to continue relying on tried and tested methods.

Modelling has been used to design components of, or whole individual unit operations in, the primary processing of pharmaceuticals. Solubility prediction of organic molecules in common solvents is becoming increasingly more accurate,(Boobier et al., 2020; Vermeire et al., 2022; Lovette et al., 2022; Vassileiou et al., 2023) and application of these models has been demonstrated to inform solvent selection for continuous crystallisation and isolation operations (Ottoboni et al., 2021; Brown et al., 2018). In the recently reported digital design of a batch crystallisation of an active pharmaceutical ingredient (API) from Takeda Pharmaceuticals International Co., an *in silico* DoE linked the CPPs to the CQAs of the crystallised product, enabling efficient process optimisation (Szilágyi et al., 2022). In another study digital design principles were used to efficiently develop integrated filtration and washing operations, using mathematical

models to facilitate isolation scenario selection (Ottoboni et al., 2022). By removing the need for trial-and-error experimentation, these applications of digital design highlight the resource reduction achievable in the development of individual unit operations. A gap remains in the use of digital design tools for initial process design and development through to manufacturing of the final, in specification, material.

Here we present our work towards a universal digital-first approach for holistic process development over a series of unit operations (crystallisation, filtration, washing and deliquoring) to engineer high quality particles of the API mefenamic acid (MFA). To demonstrate the ability to selectively design product attributes and modulate particle size, two distinct D_{90} sizes (42 µm and 120 µm) were selected as targets based on biopharmaceutical performance models to assess their effect on product performance. The accuracy of state-of-the-art models is assessed to identify challenges in their application or performance for further development to enable a fully integrated digital-first design approach.

1.1.   *Chosen API system*

MFA is the API used to demonstrate our process development activities. MFA is a Biopharmaceutics Classification System (BCS) Class II non-steroidal anti-inflammatory used in tablet form to treat mild to moderate pain (Cimolai, 2014). Typically, polar aprotic solvents are used for cooling crystallisations of MFA such as acetone, dimethylsulfoxide (DMSO) or *N,N*-dimethylacetamide (DMA),(Cesur and Gokbel, 2008) as protic solvents (*e.g.* ethanol) report lower product yields (Sharma and Gogate, 2020) and the use of *N,N*-dimethylformamide (DMF) can lead to solvate formation or metastable forms being isolated (Cesur and Gokbel, 2008; SeethaLekshmi and Guru Row, 2012). Crystallographically MFA has three possible polymorphic forms, stable form I and metastable forms II and III, which can interconvert thermally.(SeethaLekshmi and Guru Row, 2012) MFA has low aqueous solubility and therefore requires a small API particle size to facilitate oral bioavailability. The hydrophobicity of MFA and its propensity to adhere to surfaces are also known to present significant processing challenges, including fouling on surfaces such as *in situ* probe surfaces and reactor walls, resulting in transfer line blockages or impacting on heat transfer (Cesur and Gokbel, 2008).

2.   Approach and methods

Fig. 1 provides a schematic overview of this work. For each operation developed, a digital-first approach was used, *i.e.,* initial modelling work informed experimental undertaking, and the main objective of all experiments was to validate and refine the final model parameters. Adopting QbD principles, initial quality targets are selected for the manufacturing process of MFA to ensure the product tablet performs as intended. As MFA is a dissolution-rate limited drug, a particle size target was used, and two target D_{90} sizes of 42 and 120 µm were selected. With consideration to the overall manufacturing process 2-butanol was selected as the optimal solvent for the crystallisation processes being developed. With the feed composition determined a population balance model (PBM) accounting for nucleation, growth and dissolution phenomena was constructed, and the appropriate crystallisation modes to achieve the particle size
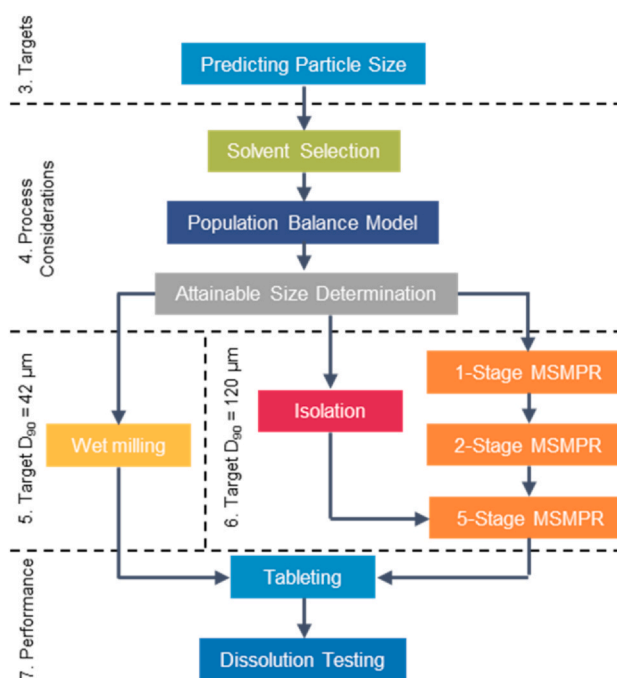

Fig. 1 – Summary of operations designed digitally and experimentally demonstrated in this work, related to the sections in which they are presented.

targets were selected using a range of attainable sizes calculations. To manufacture particles with a D_{90} of 42 µm, a wet milling process was developed and demonstrated. To manufacture particles with a D_{90} of 120 µm a 5-stage mixed suspension–mixed product removal (MSMPR) process was targeted. This is a more complex process where not all possible phenomena can be modelled (*i.e.*, transferring slurry between vessels, fouling/encrustation *etc.*), and therefore validation of the model required preliminary 1-stage and 2-stage MSMPR experiments before moving to MFA manufacture. A continuous isolation procedure was developed in parallel to the crystallisation processes and enabled the filtration, washing and drying of the MFA product. The performance of both MFA product batches was determined and compared by measuring the dissolution properties of resulting tableted particles.

The models presented throughout this work were implemented using gPROMS FormulatedProducts® (gFP). As research activities were conducted at geographically separate sites multiple software versions were used throughout (Table S1). To prevent duplication of symbols denoting properties and parameters for the integrated process systems, some standard equations and models are presented with modified terms, the addition of a subscript correlating to the model type in most cases.

A summary of the experimental characterisation methods used in this work are listed in Table 1. For brevity, detailed experimental methods for this work have been included in the supplementary information.

Throughout this work, the D_{90} particle size is defined as the volume weighted 90th percentile of a particle size distribution. All implemented models and experimental measurements use this definition of particle size D_{90}. Seed particle sizes are described using the conventional $D_{4,3}$ value, the volume weighted mean value of a particle size distribution (ISO 9276–2, 2023).

Table 1 – Summary of methods used to measure specific properties and characterise crystallisation product batches throughout this work. Experimental details of each technique can be found in the supplementary information.

MFA solubility (solvent screen)	Turbidity
In-line particle size and number	Focused beam reflectance measurement (FBRM) and particle vision and measurement (PVM)
In-line MFA concentration	Ultraviolet (UV) spectrometry
Off-line Particle size, D_{90}	Laser diffraction (slurry) or optical microscopy (dried powder dispersed with compressed air, circle equivalent (CE) diameter)
Off-line MFA concentration	UV spectrometry
Polymorphic form	Powder X-ray diffraction (PXRD)
Moisture content	Loss on drying (LOD)

During both manufacturing runs, process analytical technology (PAT) was used for in-line monitoring. The wet-milling process was monitored using an *in situ* focused beam reflectance measurement (FBRM) probe to measure the chord length distribution, which was converted to an estimated particle size distribution for initial model parameterisation experiments (Agimelen et al., 2016; Ferreira et al., 2020). Slurry samples were taken during model validation and manufacturing process operation where the particle size distribution (PSD) was measured using laser diffraction methods, from which a D_{90} value was extracted. Similar measurements were conducted for the product particles.

The MSMPR processes were monitored by ultraviolet (UV) spectrometry, FBRM and particle vision and measurement (PVM) to measure the process attributes of solute concentration (C_{Cryst}), number of crystals and estimate particle size respectively. The final configuration chosen was within constraints imposed by practical limitations (*e.g.* vessel configurations, port accessibility, equipment availability) and detailed discussion of the optimal probe placements is out of scope here. Sampling was also undertaken during the MSMPR processes to determine the solute concentration by off-line UV spectrometry, as well as to determine the particle size D_{90}.

3. Selecting/ predicting quality targets

Mefenamic acid (MFA) has poor aqueous solubility and high permeability, with dissolution rate limited absorption of the drug into the body (Butler and Dressman, 2010). For dissolution rate limited drugs, formulation approaches need to carefully consider the polymorphic form, (Romero, 1999) particle size, surface area and wettability of the drug to achieve complete oral absorption (Butler and Dressman, 2010; Vasconcelos et al., 2007) (*i.e.*, the time taken for > 90% of the API to dissolve in the body). In terms of particle size, the D_{90}, whilst challenging to control from a manufacturing standpoint, is used in these cases as larger particles will heavily influence the particle dissolution timeframe. To determine the particle size required to achieve complete oral absorption, several approaches were taken: (1) based on the Developability Classification System (DCS), a particle size (D_{90}) of 42 μm was calculated as sufficient to achieve complete oral absorption of MFA (*in vivo*) at the therapeutic dose of 250 mg (assuming 500 mL intestinal volume and a gastrointestinal (GI) transit time of 3.32 h) (Butler and Dressman, 2010). (2) Refined DCS by Rosenberger and co-workers, (Rosenberger et al., 2018) implemented in BASF ZoomLab™, (BASF SE, 2021) which calculates a particle size of $D_{90} = 60$ μm to achieve complete oral absorption for the same therapeutic dose. (3) An oral absorption model (Human GI tract, gFP),
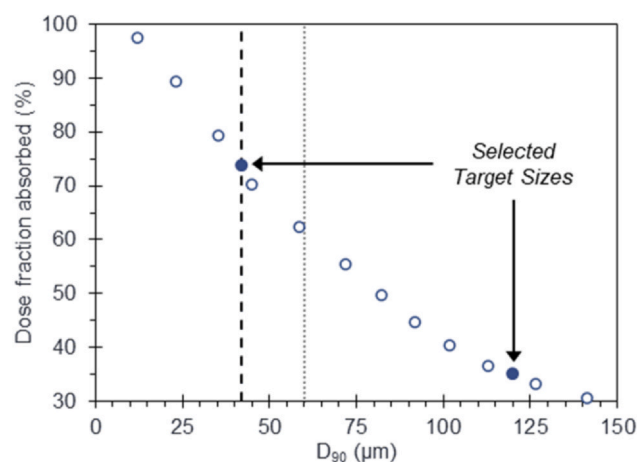

Fig. 2 – Variance of MFA dose fraction absorbed with particle size (D_{90}). (○) gFP oral absorption model, dashed lines indicating literature values using (– –) developability classification system(Abuhassan et al., 2022) and (⋯⋯) BASF ZoomLab™.(BASF SE, 2021).

assuming fasted digestive state, 220 min small intestine residence time) was also developed using the solubility of MFA as a function of pH and bile concentration (TenHoor et al., 1991; Abuhassan et al., 2022). Comparison of these calculations of oral absorption are shown in Fig. 2.

From the gFP oral absorption model a D_{90} of 12 μm would be required to achieve greater than 95% oral absorption, in contrast to the DCS calculations of 42 and 60 μm. Therefore, as a compromise between this range of sizes, we targeted the preparation of MFA particles with a D_{90} of 42 μm. To further demonstrate the digital first approach, a second larger particle was also to be prepared, with a D_{90} of 120 μm (Fig. 2). This would provide a sufficient contrast to material with a D_{90} of 42 μm, with a measurable decrease in dissolution during final product *in vitro* testing and provide an additional target for the crystallisation development. It follows that the modelled dissolution curves for the two particle sizes are expected to be distinct, with a high difference factor, f_1 of 35.8 and low similarity factor, f_2 of 19.1 (section S2.2.3 and Table S50).

Attaining specific particle sizes is the primary target of the processes developed in this work. Other product attributes are also measured, with the objective to meet established quality specifications. As no impurities are present during the operations developed (Section 4.1), a sufficiently high product chemical purity is assumed. To meet the European Pharmacopoeia specification, the crystallised particles must be phase pure MFA form I and free from volatiles, with a loss
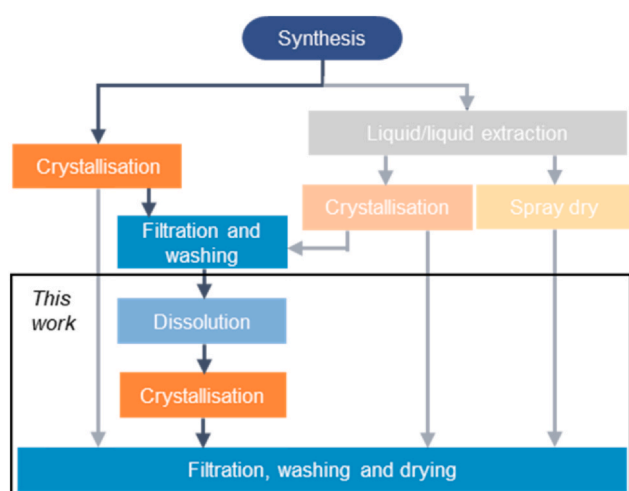
Fig. 3 – Schematic depicting the different process scenarios considered, with the chosen route highlighted. Specific processes developed in this work are the second crystallisation and final filter, wash and dry.

on drying (LOD) value less than 0.10%. (Mefenamic Acid Specification, 2023)

4. General process considerations

4.1. Upstream processes

Prior to the crystallisation of MFA for particle engineering to meet the desired particle attributes, an upstream process for the synthesis and initial purification of MFA was considered. Currently the manufacture of MFA is a batch process with long batch times and uses hazardous DMF as a solvent. In collaboration with our industrial partner,(Snapdragon Chemistry Inc) the feasibility of a continuous flow chemistry synthesis route was explored, and a base-catalysed Ullmann coupling(Sambiagio et al., 2014) of 2-chlorobenzoic acid with 2,3-dimethylaniline in a diglyme/water solvent mixture was developed. The final stream was composed of unreacted reagents, benzoic acid (a degradation product of 2-chlorobenzoic acid) and MFA. Following synthesis several workup scenarios were explored, these ranged in complexity from a telescoped crystallisation directly after synthesis, through to a liquid/liquid extraction followed by a crystallisation (Fig. 3). These scenarios were scored through a multicriteria decision making framework(Hodgett, 2013; ChemDecide, 2023) considering the potential product purity, process robustness, process efficiency, resources required to develop and process complexity. The best compromise was found to be telescoping of an antisolvent (with water as antisolvent) crystallisation from the synthesis output stream, followed by a second crystallisation to control particle size. Assessment of impurity rejection for the initial crystallisation was performed for 2-chlorobenzoic acid, benzoic acid and 2,3-dimethylaniline and found that rejection of all impurities was high and crystals of mefenamic acid of high purity were produced.(Urwin et al) Therefore, most of the purging of impurities from this upstream process occurs during filtration and washing. Small-scale filtration studies were performed to measure the cake resistance and used to estimate the final wet cake composition under several wash volumes, deliquoring and wash solvent scenarios.(Ottoboni et al., 2022) In the worst-case scenario of 3 washes each with 1

Table 2 – Mass fractions of filter cake from first isolation process and its dilution with 2-butanol. Water, 2-chlorobenzoic acid, benzoic acid and 2,3-dimethylaniline are present in trace amounts.

	Mass Fraction	
	Filter Cake	After Dissolution
Mefenamic Acid	0.5015	0.0910
n-Heptane	0.4723	0.0857
Diglyme	0.0222	0.0040
2-Butanol	—	0.8186

equivalent cake volume of n-heptane, followed by deliquoring to a residual solvent fraction of 0.5, the final filtration cake consisted of mefenamic acid ($X_{MFA} = 0.5015$), n-heptane ($X_{Hept} = 0.4723$) and diglyme ($X_{Dig} = 0.0222$), with water, 2-chlorobenzoic acid, benzoic acid and 2,3-dimethylaniline in trace amounts (total < 0.4 w%, Table 2). This filtration cake is the input material for the particle engineering crystallisation, the first step of which is dissolution into an appropriate solvent for the process.

4.2. 4.2 Solvent selection for crystallisation

For crystallisation solvent selection, solvents for screening were restricted to ICH class 3 (solvents with low toxic potential) solvents,(ICH, 2011) as well as those that are chemically compatible with the equipment wetted materials of construction. The solubility curves for the shortlisted 26 solvents were calculated using COSMOtherm (Section S3.1). (BIOVIA) For all solvents 5 °C or a MFA concentration of $X_{MFA} = 0.005$ was chosen as the lowest (end of process) temperature.(Black and Muller, 2010) The saturated temperature was chosen as the temperature required to achieve > 90% yield or the solution boiling point minus 10 °C, whichever is lowest, whilst maintaining the product solid mass fraction less than or equal to 0.25 to enable processability. With these points defined, the theoretical yield operating between these two points was determined.(Brown et al., 2018) From the difference between the initial and final concentrations the mass fraction of solids present in the product and an estimated throughput for a given solvent flow rate (*e.g.* 50 g min^{-1}) were also calculated.

When compared against established selection criteria, (Brown et al., 2018) 8 solvents were considered as suitable potential crystallisation solvents (Fig. S1); 2-pentanol, 1-butanol, 2-butanol, isobutanol, cyclopentyl methyl ether (CPME), 2-methyltetrahydrofuran (2-MeTHF), isobutyl acetate and propyl acetate. Experimental validation of the predicted solubilities and qualitative assessment of the crystallisation behaviour at small-scale was performed in 8 mL vials, monitored using a turbidity probe and in-line camera (Fig. S2). Of the candidate solvents, isobutyl acetate and propyl acetate were excluded owing to chemical incompatibility with the chosen equipment. CPME and 2-MeTHF were excluded due to their higher comparative cost to the other potential solvents. Isobutanol was not favourable as it had a low product mass fraction of solids, making the product slurry difficult to process in continuous filtration equipment. Of the remaining solvents (2-pentanol, 1-butanol and 2-butanol), 2-pentanol had the highest yield and estimated throughput (Table S5). However, the *in situ* imaging during the small-scale experiments showed the presence of an undesirable needle crystal

habit. 1-Butanol had the next highest yield and throughput, but similarly, *in situ* imaging showed the formation of agglomerates. Therefore, 2-butanol was selected as the preferred solvent as it showed the most consistent crystal habit during the small-scale experiments, whilst meeting the other targets and constraints.

The wet filter cake isolated from the first crystallisation was therefore dissolved into 2-butanol to create a feed stream into the final crystallisation for particle engineering (Table 2). For estimation and validation experiments, this feed stream composition will be recreated. To achieve this sufficient 2-butanol was added to target an MFA concentration of $X_{MFA} = 0.0910$. Given the minimal amount of diglyme remaining in solution after solvation with 2-butanol, the solvent composition for the final crystallisation development was approximated to a 2-butanol/n-heptane (90:10 w/w) mixture containing MFA, $X_{MFA} = 0.0910$.

4.3. Crystallisation mode selection

A crystallisation process consists of nucleation, growth, dissolution, agglomeration and breakage phenomena. Whilst the separation of these highly coupled mechanisms to estimate the many encompassed parameters poses a significant challenge, experiments designed to perform sequential parameter estimation have been reported.(Pérez-Calvo et al., 2016; Wohlgemuth and Schembecker, 2013) From this, a sequential parameter determination captures and optimises the dominant process mechanisms to achieve targeted quality attributes by minimising or maximising nucleation, growth or agglomeration in a continuous crystallisation process. For this work, models based on first principles were built by fitting the kinetic parameters to these well-designed experiments that isolate individual size-change mechanisms. The mathematical model was then validated against data from batch temperature cycling experiments under direct nucleation control (DNC) and continuous MSMPR crystallisation experiments.

4.3.1. Crystallisation population balance model
Sequential parameter estimation has been widely adopted in the literature and the established methods were used here. (Pérez-Calvo et al., 2016; Bari and Pandit, 2014; Bari et al., 2017; Bari and Pandit, 2018; Andreassen and Hounslow, 2004) The kinetic parameters for primary nucleation, secondary nucleation, growth and agglomeration were estimated from experimental data. Breakage phenomena were omitted as little crystal breakage has been observed in processes targeting similar, reasonably small particle sizes. The selection of kinetic expressions for crystal growth and secondary nucleation can strongly influence the quality of the model fit achieved. (McGinty et al., 2020) The driving force for depletion of solute concentration in solution is expressed as the absolute supersaturation S_{Cryst}, the difference between solute and equilibrium concentration, C_{Cryst} and C^* respectively, Eq. (1).

$$S_{Cryst} = C_{Cryst} - C^* \tag{1}$$

In an unseeded process, spontaneous primary nucleation occurs at high S_{Cryst} values. The primary nucleation rate J_1 is given by Eq. (2), where k_{b_1} is the primary nucleation rate constant and b_1 is the primary nucleation order.

$$J_1 = k_{b_1}(S_{Cryst})^{b_1} \tag{2}$$

The presence of these initial particles induces secondary nucleation, which can be caused by inter-crystal attrition or crystal collision with hard surfaces, such as the impellor. Crystal-crystal collisions were not considered here as the low solubility of MFA dictated a low feed concentration and leads to a low solid content in the resulting product slurry, and hence low attrition rates between crystals were expected. Eq. (3) defines the secondary nucleation rate J_2 where crystal-impellor collisions are the main source of attrition,(Evans et al., 1974) where k_{b_2} is the secondary nucleation rate constant, b_2 is the secondary nucleation supersaturation order, accounting for the flow number N_Q and power number N_P of the impellor. These collisions are dependent on the slurry density ρ_s, the slurry density order m, the energy dissipation rate ε_{PBM}, the density of particles n and their volume shape factor k_v.

$$J_2 = k_{b_2}(S_{Cryst})^{b_2}\frac{N_Q}{N_P} \quad k_v\rho_c\varepsilon_{PBM}\int_{L_{min}}^{\infty} nL^3 dL \tag{3}$$

Crystal growth depletes the concentration of the solute in solution, and as such is the dominant force in a crystallisation, affecting the supersaturation profile and particle size. This power law based growth and dissolution model is used to describe the growth and dissolution mechanisms, Eqs. (4) and (5) respectively. The growth rate, G, and dissolution rate, G_d, are related to the growth and dissolution rate constants (k_g and k_{g_d}) and the absolute concentration to the supersaturation or de-saturation order (g and g_d).

$$G = k_g(S_{Cryst})^g \tag{4}$$

$$G_d = k_{g_d}(S_{Cryst})^{g_d} \tag{5}$$

The crystallisation kinetic parameters were estimated in an optimisation routine by minimising the difference between experimental data and model simulation results for the same experiments. The kinetic models selected together with the physical properties, the solubility curve and the assumption of a perfectly mixed suspension were introduced into the modelling platform. To perform the optimisation, techniques using the finite-volume method were employed to solve the population balance equations (PBE) in gFP. The parameter estimation tool in gFP was used for simultaneous estimation of multiple parameters.

The particle size grid setting and variance function to solve the PBE can affect the values of the model parameters and build the PBM. A preliminary investigation of particle size grid setting indicated that the simulated particle size approaches the real particle size when the number of grids is above 50. Below 50, the particle size is weighted towards larger sizes and fails to account for the small sized particles. A particle size range of 1–1000 μm was chosen, which corresponds to the detectable particle size range from the process monitoring methods used during the experimental crystallisation process.

4.3.2. Modelling parameters
Table S6 describes the full experimental plan to estimate and fit all parameters within the PBM described. The comparison between different kinetic mechanisms allows the suitability of the assumptions and experimental conditions chosen for the decoupling of the different crystallisation phenomena to be assessed.

To minimise the effect of secondary nucleation during estimation of growth parameters, a slow cooling temperature profile with isothermal holds was used to mitigate secondary

Table 3 – Crystallisation model parameter estimation results with 95% confidence intervals.

Kinetic Component		Value	Confidence Interval	Unit
Growth	k_g	5×10^{-4}	8×10^{-4}	µm/s
	g	1.56	0.202	-
Dissolution	k_{g_d}	2×10^{-3}	9.5×10^{-4}	µm/s
	g_d	1.56	-	-
Secondary nucleation	k_{b_2}	19.7	5.53	Ln(#/m³·s)
	b_2	2.14	10.2	-
	l_{min}	206	1.4×10^{-3}	Mm
Primary nucleation	k_{b_1}	1.77	0.969	#/m³·s
	b_1	26.4	123.696	-
Agglomeration	A_{50}	0.01	0.590	N/m

nucleation (Fig. S7). A relatively constant FBRM total counts value indicated that the formation of secondary nuclei is supressed under operation at a low supersaturation level, generated using small steps in the cooling ramp. Further, a low stirring rate agitates the crystals into a homogeneous state as there was little solid content in the growth test experiment. A moderate stirring speed can also limit crystal-impellor or crystal-crystal collisions.

Solute concentration and particle size (D_{10}, D_{50} and D_{90}) were used as data input during all parameter estimation processes. In typical parameter estimation, a single size input (*e.g.* mean size) is used, however inclusion of the D_{10} and D_{90} allows for a more detailed size distribution to be modelled. This also created the additional challenge to obtain the optimum fitting parameters. Table 3 summarises the estimated kinetic parameters, further validation was then performed through batch temperature cycling and continuous multi-stage crystallisation experiments.

4.3.3. *Validation*

The mathematical model was then validated against data from batch cooling and DNC experiments, with a cyclic heating-cooling temperature (T-cycling) profile. Over the sequential temperature cycles, the simulated and experimental decreases in MFA solution concentration are in good agreement (Fig. 3a). Similar comparison of the particle sizes throughout the experiment (Fig. 3b) show a good fit between the simulated and experimental D_{50} values, but slight deviation for D_{10} and D_{90} values. The model predicts the median values well but is not as accurate at the extremes of the range. The model implemented in gFP assumes equal growth and dissolution rates, which is not the case for the crystallisation of MFA in 2-butanol/*n*-heptane (90:10 w/w) ($k_{g_d}= 2 \times 10^{-3}$ µm s⁻¹; $k_g = 5 \times 10^{-4}$ µm s⁻¹). Constrained to a single value, the k_g value was used to model the evolution of particle size, leading to discrepancies in fit at the extremes of the range.

Further batch crystallisations using T-cycling validated data from unseeded DNC experiments were extended to validate the kinetic parameters for primary and secondary nucleation, growth and dissolution processes. In all unseeded batch experiments, the final product morphology shows very little agglomeration.

4.3.4. *Attainable particle sizes*

In order to explore possible crystalliser configurations (*e.g.* number of stages in an MSMPR cascade) a region of attainable sizes approach was taken to map out the range of particle sizes that would be possible to achieve within the configurable MSMPR platform.(Vetter et al., 2014) Taking the parameterised crystallisation model described previously, a GSA was performed in gFP. Using the parameterised model, discrete flowsheets for unseeded crystallisations in a 1-stage, 3-stage and 5-stage MSMPR were constructed. For each flowsheet a grid search of process parameters was performed, as detailed in Table S7. Results from each grid search were then processed to determine the maximum and minimum attainable D_{90} for a thermodynamically achievable yield ≥ 90%, these boundaries are shown in Fig. 5.

The range of attainable sizes using an unseeded, multi-stage cooling crystallisation is depicted in Fig. 5a, from which two key points can be concluded: (1) the range of attainable D_{90} sizes does not significantly increase with the number of stages. However, it would be expected that configurations with a higher number of stages could potentially have lower supersaturations than those with fewer stages. In a possible 1-stage and 5-stage MSMPR setup with the same inlet and outlet concentration, the supersaturation in later vessels of the multi-stage cascade will likely be lower than the supersaturation in a single vessel process. This would be beneficial for the avoidance of fouling and encrustation. (2) None of the cascade configurations for an unseeded crystallisation result in a region which overlaps with the target D_{90} sizes of 42 µm and 120 µm. This suggested that an unseeded crystallisation (*i.e.*, relying on primary and secondary nucleation for the generation of particles) is unsuitable to deliver these particles sizes, and some external influence would be required. For the smaller size (D_{90} = 42 µm) a wet milling approach was chosen to explore this, as this has previously been shown to be capable of delivering particles in the sub 50 µm range. (Meng et al., 2020) For the larger size (D_{90} = 120 µm) using a continuous seeded cooling crystallisation was explored, using the maximum number of MSMPR vessels practically available (5). Applying the same range of attainable sizes approach (Fig. 4b), using seeds with a $D_{4,3}$ size of 30 µm we can access a final MFA D_{90} particle size of 120 µm using a 5-stage MSMPR cascade.

5. Target particle size $D_{90} = 42$ µm

In the context of continuous crystallisation, the integration of wet media milling technologies, particularly rotor-stator devices, has been shown to prevent common product issues encountered with traditional dry milling units. High energy milling alleviates challenges such as the introduction of crystal lattice disorder, undesired polymorphic/amorphous transformations and broad bimodal product particle size distributions.(Agimelen et al., 2018; Ahmed et al., 2019; Szilagyi and Nagy, 2019) It is also beneficial in terms of reduced operator exposure to high potency APIs, improves yield and process control and decreases energy cost.

To obtain MFA with a particle size, D_{90}, of 42 µm, we explored the region of attainable particle sizes based on the performance of a wet milling model, with a focus on developing a mechanistic model to describe the wet milling process. Breakage kinetics were parameterised to optimise the milling performance and explore the effects on downstream processes, such as crystallisation. A secondary objective of the wet milling process was to generate seed material which could be used later in the preparation of larger particle size
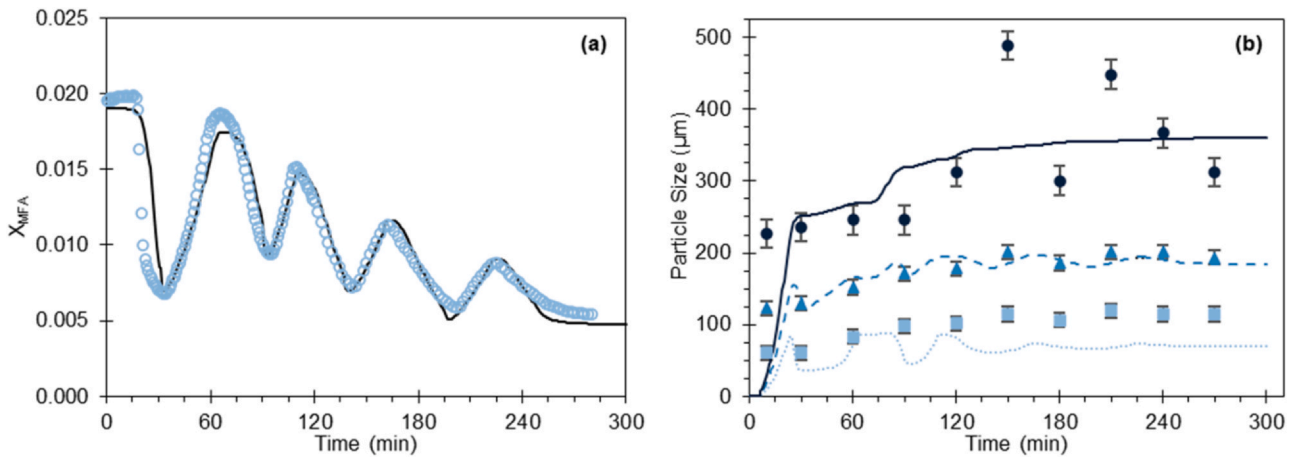
Fig. 4 – (a) Comparison of experimental (○, measured *in situ*) and predicted (—) X_{MFA} during one of the DNC crystallisations to determine nucleation kinetics. **(b)** Comparison of experimental (points, measured *in situ* using a combination of FBRM and PVM) and predicted (lines) particle size (●; ■; ·····) D_{10}, (▲; – –) D_{50}, (●; —) D_{90} for during the batch crystallisation to determine agglomeration kinetics.
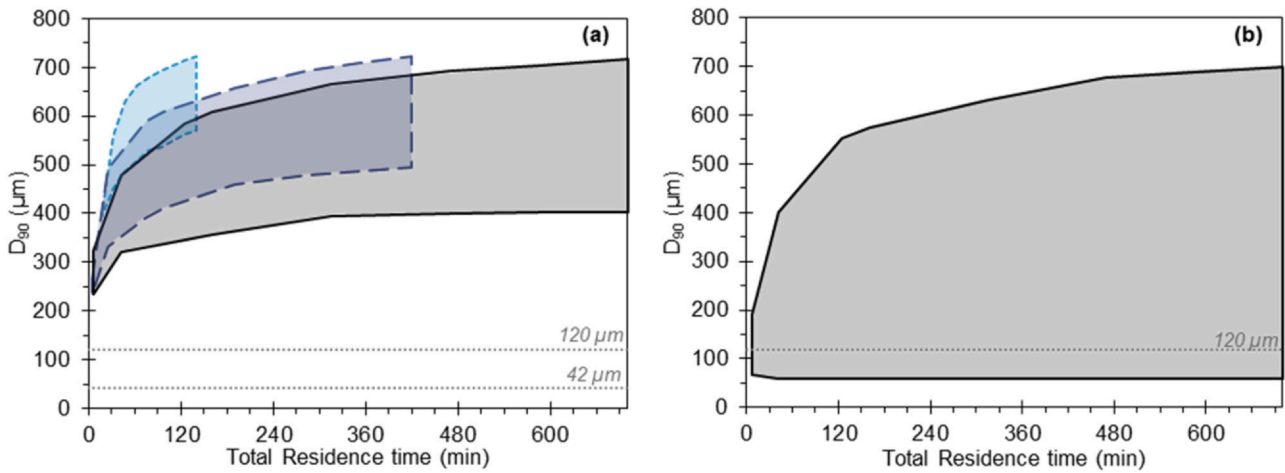

Fig. 5 – Ranges of attainable particle sizes *via* cooling crystallisation under (a) unseeded conditions, (- -) 1-stage MSMPR, (– –) 3-stage MSMPR, (—) 5-stage MSMPR and (b) seeded conditions in a 5-stage MSMPR setup with a seed size $D_{4,3} = 30\,\mu m$. For other seed sizes see Fig. S8.

MFA through a continuous seeded cooling crystallisation process.

5.1.   *Wet milling model development*

A single wet milling experiment identified the smallest possible particle size that could be achieved using the standard mill configuration (Fig. S9). Using this value, an initial model was developed using gFP, using the built-in wet milling population balance model. This gives the breakage kinetics Eqs. (7) and (8). (Austin et al., 1976) This includes γ_{WM}, β', ϕ and α' as kernel parameters, ω and y are breaking particle volumes and corresponding sizes (m^3 and μm), υ and x are product particle volumes and corresponding sizes (m^3 and μm), $\omega_{critical}$ and $y_{critical}$ are critical volumes and corresponding sizes that prevent particle from further breakage and Sc_M is the constant rate of breakage at critical size (s^{-1}).

$$B_M(\upsilon, \omega) = \phi_{WM}\left(\frac{\upsilon}{\omega}\right)^{\frac{\gamma_{WM}}{3}} + (1 - \phi_{WM})\left(\frac{\upsilon}{\omega}\right)^{\frac{\beta'}{3}} \quad (7)$$

$$S_M(\omega) = \begin{cases} Sc_M\left(\frac{\omega}{\omega_{critical}}\right)^{\frac{\alpha'}{3}} & for \quad \omega \geq \omega_{critical} \\ 0 & for \quad \omega < \omega_{critical} \end{cases} \quad (8)$$

The linear correlation between breakage rate (S_{WM}) and shear rate (C_{WM}) is given by Eq. (9). (Karabelas, 1976)

$$S_{WM} = C_{WM}\gamma_{WM} \quad (9)$$

For rotor-stator wet mills, the equation can be generalised to include gap thickness between the rotor and stator, and the rotor frequencies (Eq. (10)), where $\upsilon_{ts,t}$ is rotor/impellor tip speed ($m\,s^{-1}$), δ is horizontal gap between rotor and stator (m), C_0 is the intercept parameter (s^{-1}) which accounts for additional breakage that may occur as the tip speed tends to zero and $N_{\gamma-\delta}$ is the number of rotor-stator rows.

$$S_{WM} = C_{WM} \sum_{i=1}^{N_{\gamma-\delta}} \frac{\upsilon_{ts,t}}{\delta_i} + C_0 \quad (10)$$

In situ chord length measurements recorded in the crystalliser vessel were converted to volume mean lengths in parameterisation experiments. (Agimelen et al., 2016;
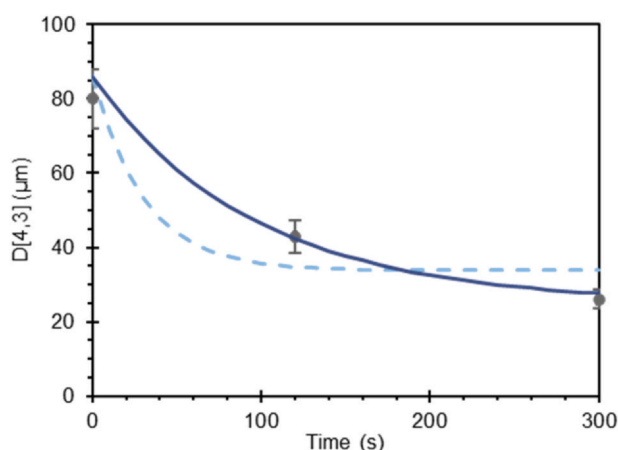
Fig. 6 – Measured *vs* predicted volume mean particle sizes for the wet mill process. (‒ ‒) Initial prediction, (———) final prediction and (●) measured values.

Fig. 7 – GSA results for particle size variation over time and with varying rotational mill speeds. (‒ ‒△‒ ‒) 3000 rpm; (‒ ‒□‒ ‒) 6000 rpm; (‒ ‒◇‒ ‒) 9000 rpm; (‒ ‒○‒ ‒) 12000 rpm; (———▲———) 15000 rpm (———■———) 18000 rpm and (———◆———) 20000 rpm.

Ferreira et al., 2020) These were used to estimate the kinetic parameters in Eqs. (7) to (10). The critical particle size was fixed at the smallest value recorded at the end of the experiment. For initial estimation of parameters, the particle size $D_{4,3}$ was used in place of the D_{90}, as this is how the commercial model used was designed to be implemented.

Based on the fit from the single experiment, further experiments with two key changes were conducted to allow a more robust and wider exploration of the design space. A coarse rotor-stator mill setup was used for re-validation of the equipment correlation and the rotational speed was varied between 3000 and 26000 rpm.

5.2. Model verification

The Austin parameter (α) (Table S9) is used to define a breakage distribution function that incorporates a critical value which physically represents the onset of plasticity effects at very small particles sizes preventing further breakage from occurring, and was determined to be 0.349 here. The Kapur parameter (q) provides a correlation for the fragmentation rate as a function of particle volume and was determined to be 0.883 here. The objective function directly quantifies the fit between predictions and experimental data and should be minimised. A value of 7.33 indicates a well-fitting model. The predicted values from the final model and experimental data are consistent, within experimental errors (Fig. 6).

This demonstrates the ability to predict and verify a model-based design approach for design and development of a wet milling process to target a specific small particle size. A single experiment was used to estimate breakage kinetics in a wet mill mechanistic model, which once validated was used to explore the design space and suggest further experiments with different rotor-stator configurations. The new experiments were shown to fit well with earlier estimated breakage kinetics, despite the change in mill configuration. Predictions were good for both the fine and coarse generators, prompting a wider design space exploration for different mill configurations.

5.3. Exploration of design space

A GSA study was used to obtain a region of attainable particle sizes. This would lead to a better understanding of mill
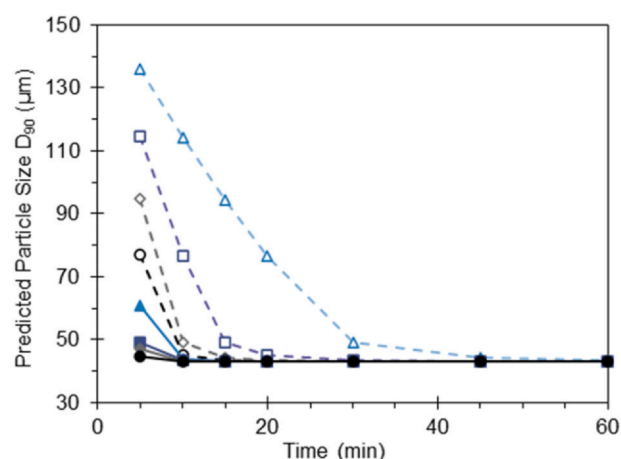
characteristics, and hence reduce the need for practical trial and error experiments to obtain the required particle size. Initial GSA results (Fig. 7) show how particle size decreases with time and different rotational speed when milled using the fine generator. It is noted that the model currently does not distinguish between different rotor-stator generators.

The GSA results suggest that lower milling rates lead to a more gradual decrease in particle size than at higher rates. Whilst this can be predicted using other methods, the use of GSA here proposes that most of the size reduction occurs in the first 15 min of the experiment and there is very little variation in particle size after milling for 30 min irrespective of rotational speed. Using this insight, further experiments were completed using the coarse generator with 13 rotor-stator teeth with rotational speeds of 3000, 6000, 12000, 18000 and 26000 rpm (Fig. S10a), where particle sizes were measured using off-line laser diffraction on slurry samples taken during the experiment. Process reproducibility was demonstrated by duplication of the experiments at 12000 and 26000 rpm (Fig. S12).

The results from these experiments were added to the model and validated, the comparison between the new predicted values and experimental results are shown in Fig. 8. The fit for the higher rotational speed experiments was good (*e.g.,* D_{90} after 10 min: 107.0 µm predicted, 107.1 µm experimental; D_{90} after 30 min: 73.2 µm predicted, 88.9 µm experimental), even though this encompassed a shift to a different mill generator (coarse generator *vs* fine generator). For the lower rotational speeds, the model significantly overpredicted the reduction in particle size achievable using this wet milling setup. From these results, a more rigorous GSA study was completed to obtain a region of attainable sizes and suggest the most appropriate and efficient experiment conditions to achieve the desired D_{90}.

The range of attainable particle sizes by varying rotor frequency are shown in Fig. S13 using (a) coarse, (b) medium and (c) fine rotor-stators. The contour plots (Fig. S13) show the desired particle size, *i.e.,* a D_{90} of 42 µm, is achievable using any of the three generators, with the fine generator achieving this in the shortest time frame (30–60 min). When considering lab-scale experimental design, the process must have a high probability of achieving the required particle size
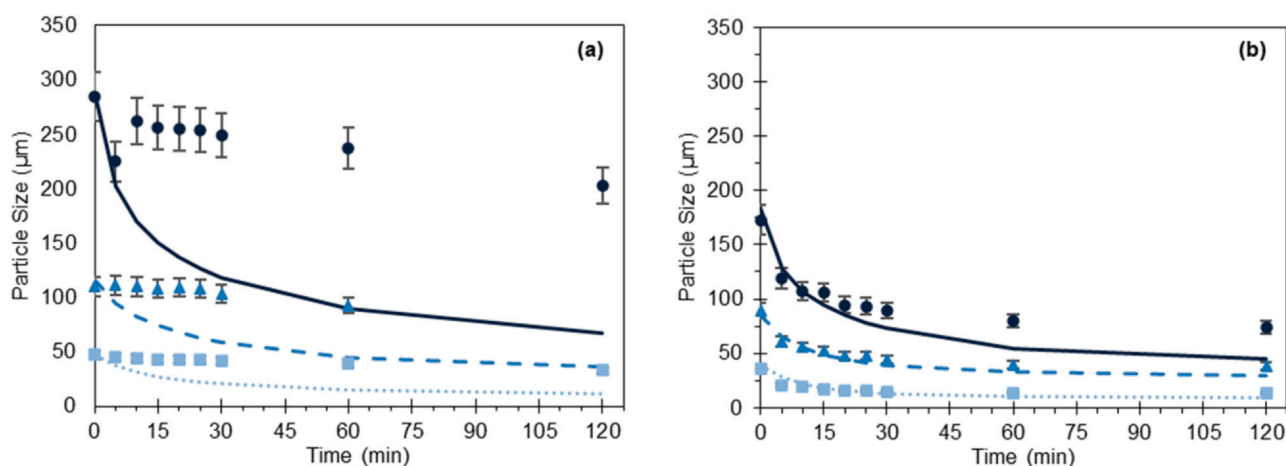
Fig. 8 – Results from wet milling model validation experiments at (a) 6000 rpm and (b) 18000 rpm, showing predicted D_{10} (■), measured D_{10} (■), predicted D_{50} (▲), measured D_{50} (▲), predicted D_{90} (–) and measured D_{90} (●).

using the most efficient rotor-stator configuration based on energy dissipation and number of rotor-stator teeth. The effect of potential experimental error on the length of the experiment should also be accounted for. From these requirements, the suggested experimental process uses a fine rotor-stator mill configuration with high rotational speeds between 18000 and 26000 rpm for a duration of 60 min.

5.4. Manufacture of D_{90} = 42 μm particles

A production run to manufacture MFA particles was undertaken using the digitally designed process. A suspension of MFA was milled using a fine rotor-stator configuration operating at 26000 rpm for 120 min, and no significant blockages or fouling issues were encountered. In-line FBRM measurements demonstrated the expected reduction in particle size, reaching the minimum value after approximately 30 min (Fig. S14). The suspension was filtered, washed and dried and the isolated powder was confirmed to be MFA form I (Fig. S15), with an acceptable LOD value of 0.08% (Table S11). The measured particle D_{90} sizes are consistent across the initial slurry and isolated powder samples, 48.3 μm and 49.5 μm respectively (Table S12), within instrumental error for the D_{90} targeted (42 μm). Further, the associated unimodal PSDs have low span values (1.46 and 1.15 respectively), indicating a narrow distribution and uniform particle size, which is visually evident in microscopy images (Fig. 9) captured of the bulk powder. Overall, the wet milling production
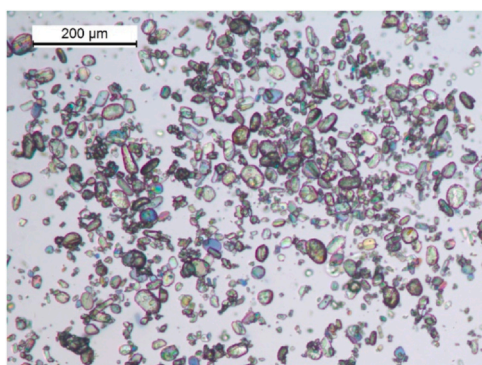
run successfully delivered 90 g of MFA product with the specified quality attributes.

The particle size of the material produced ($D_{4,3}$ = 34.1 μm) is predicted to be a suitable seed size to obtain larger MFA target particle size (D_{90} = 120 μm) through a 5-stage MSMPR cascade (Fig. 5b). Therefore, for the seeded cooling crystallisation process, these generated small particles will be used as seed material.

6. Target particle size D_{90} = 120 μm

Following the earlier development of the PBM and crystallisation mode selection, a 5-stage MSMPR seeded cooling crystallisation using 2-butanol/n-heptane as the solvent system was developed to produce MFA particles with a D_{90} of 120 μm. This was achieved through first designing the required isolation operations (filtration, washing and drying), followed by development of the required analytical and sampling methods, then sequential 1-stage and 2-stage experiments and finally a 5-stage manufacturing process.

6.1. Isolation model development

Following the seeded cooling crystallisation, the MFA product must be isolated, without excessive dissolution of the API, precipitation of impurities or agglomeration of the particles. The individual unit operations of product filtration, displacement /diffusion-dispersion washing processes and deliquoring are commonly combined into a single isolation process. (Ottoboni et al., 2022) Using the conditions generated during the upstream crystallisation process, models were developed and validated to identify the optimal isolation strategy to maximise cake purity, considering varied input material properties (particle size distribution, solid loading and liquid phase composition) to provide operating condition tolerance. The model parameters are estimated and validated using batch processes, and subsequently applied to the continuous isolation procedure.

In the wider MFA end-to-end manufacturing process, filtration and washing unit operations were already completed before the particle engineering operations developed in this work (Fig. 3). The intermediate MFA product was crystallised from a diglyme/water (80:20 w/w) solvent mixture, for the purpose of purging impurities. Due to process development work occurring in parallel, the batch isolation model

Fig. 9 – Microscopy image of MFA product isolated from milling production run.

presented here was developed using the first crystallisation outlet stream as the starting suspension, *i.e.,* using a diglyme/water solvent system in the presence of 2-chlorobenzoic acid (CBA). Demonstrating the transferability of digital process development, the results are directly implemented into the continuous isolation model required for the particle engineering seeded cooling crystallisation without repetition of experiments.

6.1.1. Wash solvent selection

Applying our previously reported wash solvent selection workflow (Ottoboni et al., 2021) to the post-crystallisation stream composition (Table 2), *n*-heptane and cyclohexane were predicted to be optimal wash solvents for the crystallised MFA product (Fig. S16). Ultimately *n*-heptane was chosen as the more appropriate wash solvent, due to its lower toxicity (ICH class 3 *vs* class 2) (ICH, 2011) and better material compatibility with available instrumentation (Table S14).

6.1.2. Batch parameter estimation and validation

The filtration process was initially modelled as a batch process, with an endpoint at dryland. Conventional cake filtration theory was used to model dead end filtration, (Destro et al., 2022) combining the Carman-Kozeny Eq. (11) to simulate cake resistance (α_{av}) and Darcy's law, Eq. (12), (Yu et al., 1996) to calculate filtrate flow rate ($\frac{dV}{dt}$). To account for any sedimentation during batch filtration, a derivative of Stoke's sedimentation law available within gFP was also applied.

$$\alpha_{av} = \frac{180(1 - \varepsilon_{Iso})}{\rho_s x_{sv}^2 \varepsilon_{Iso}^3} \tag{11}$$

$$\frac{dV}{dt} = \frac{A^2 \Delta P}{\mu_{Iso} \ (\alpha_{av} C_{Iso} V_{Iso} + A R_m)} \tag{12}$$

In Eq. (11) ε_{Iso} corresponds to the cake porosity, ρ_s is the solid density and x_{sv} is the particle volume equivalent diameter. In Eq. (12) A corresponds to the filter area, ΔP is the pressure drop along the filter axis, μ_{Iso} is the filtrate viscosity, C_{Iso} is the dry cake mass per unit volume of filtrate, V_{Iso} is the filtrate volume removed, and R_m is the filter medium resistance.

Construction of the filtration model employed here required estimation of α_{av}. A known fixed media resistance value is used, valid for all simulations using the API material and pore size distribution. To minimise resource requirements, experiments where iterative filtrations of the same suspension were processed with different driving forces were carried out, and the media resistance (R_m) was estimated to be 7.05×10^{-7} m^{-1} (Table S23). The cake resistance was calculated using the compressibility index at different driving forces, with an initial postulated compressibility index value of 1.64. (This value is in the range of compressibility index values characteristics of partially compressible cakes, 2023) Using this value, the cake resistance of existing experiments was re-calculated, to validate the compressibility index obtained. Discrepancies between the estimated and experimental cake resistance values were found. Therefore, the value was re-estimated with corrected values of the natural logarithm of the cake resistance, giving a refined increased compressibility index value of 1.91. This value indicates a partially-highly compressible cake. The calculated cake resistance was used to calculate the porosity (ε_{Iso}) at different driving forces using Eq. (11). These values

were used to simulate filtration outcomes (flow rate and time) and select the appropriate filtration and washing driving force for the experimental process. A series of simulations then selected the optimal filtration and washing driving force to facilitate rapid filtration, whilst allowing enough mother liquor and wash solvent mixing time. A diffusion-dilution with axial dispersion washing mechanism was modelled using Eq. (13). (Tien, 2012)

$$D_L \frac{d^2c}{dx^2} - \frac{u_s}{\varepsilon_{av}} \frac{dc}{dx} = \frac{dc}{dt} \tag{13}$$

For the initial conditions of:

$$c_j = c_{j,i} \quad x > 0 \quad t < 0 \tag{14}$$

And boundary conditions (assuming that the axial dispersion effect is ignored at the top of the cake):

$$c_j = c_{j,w} \quad x = 0 \tag{15a}$$

$$\frac{\delta c_j}{\delta x} = 0 \quad x \to \infty \tag{15b}$$

The diffusion-dispersion mechanisms of washing assumed a fixed molecular diffusivity coefficient and the axial dispersion coefficient was calculated using the methods reported by Huhtanen *et al.* (Huhtanen et al., 2012) and Tien. (Tien, 2012)

From simulations at different driving forces, an ideal driving force of 400 mbar was determined. The simulated filtration time was less than 10 s, and the simulated level of residual impurities in the cake after the first wash is sufficiently low (X_{CBA} = 0.0005) to be fully removed in the washing stage (Table S16). It is noted that a higher washing driving force gave higher impurity residual content in the cake at the end of wash 1.

After selecting the driving force to use during filtration, the washing strategy parameters were modelled and validated. The initial input for the washing model is the wet packed bed obtained by filtration, and the same diffusion-dispersion mechanisms as implemented previously to simulate the washing procedure. Overall, the experimental values for the solute mass fraction in the filtrate are consistent with the simulated values (Table 7), however a slight discrepancy is observed for the CBA concentration after filtration; less CBA is present than expected. The diffusion-dispersion simulation only includes MFA-specific solubility data; the solubility of other solutes is approximated to match that of the API. CBA is considerably more soluble than MFA under the crystallisation process conditions (solvent system diglyme/water 80:20 w/w: X_{MFA} = 0.0651, X_{CBA} = 0.3324), (Urwin et al) explaining why the CBA removal during washing was underestimated. More CBA remains in the residual crystallisation solvent mixture held within the cake. For the seeded cooling crystallisation developed in this work, impurity rejection is not considered, however we note that future incorporation of impurity solubility into the model would allow better estimates of impurity removal during washing. Table 4.

Next, simulations to identify an optimal washing strategy were completed (Table S17) with the target of maximising cake purity (by maximising the removal of impure mother liquor), whilst removing dissolved MFA and preventing particle agglomeration. To maximise cake purity, volumes of wash solvent were varied for a series of 3 washes. The difference between 2 and 3 equivalent cake volumes (ECV) per wash was explored. To prevent an antisolvent effect which

Table 4 – Simulated and experimental mass fraction of the species in the removed filtrate, in the case of 1 wash performed with 3 ECVs of wash solvent; washing driving force corresponds to 400 mbar. *Mass fraction of solutes, not inclusive of solvent.

	Filtrate After Filtration		Filtrate After Wash 1	
	Simulated	Experimental	Simulated	Experimental
X_{MFA}*	0.8241	0.9082	0.8228	0.8416
X_{CBA}*	0.1759	0.0918	0.1772	0.1584

would precipitate impurities, (Ottoboni et al., 2021; Shahid et al., 2021) the first wash in each scenario was a mixture of the crystallisation solvent and *n*-heptane (diglyme/water:-heptane 20:80 w/w). The subsequent wash(es) used pure *n*-heptane to minimise agglomeration during drying. Overall, the strategy selected for washing is to wash the filter cake with 3 ECVs of solvent per wash. As no kinetic models for deliquoring (drying) in batch processes are available, this unit operation was not modelled here.

6.1.3. Continuous parameter estimation, validation, and design space analysis

To transfer the batch isolation model developed for the first crystallisation to the second seeded cooling crystallisation to target a particle size D_{90} of 120 µm, the parameter estimation and validation was repeated under continuous conditions. The input material for this updated isolation model is MFA particles crystallised from 2-butanol/*n*-heptane (90:10 w/w), with no impurities present.

Following our previous methodology, (Ottoboni et al., 2022) the optimised batch crystallisation model was used as the input for the continuous isolation model, accounting for filtration, washing and deliquoring operations. The composition of the post-crystallisation stream (Table 2) was adapted for parameter estimation (Table S18). To transfer the previous isolation model from a batch to continuous process, additional parameter estimation was required for ε_{Iso} and particle sphericity. These were estimated from the batch experiments and used in a continuous filtration and washing simulation. Using the cumulative filtrate volume over time, the estimated porosity (0.309) and Carman-Kozeny sphericity (0.447) values with a good experimental fit (Table S19). There is agreement with the simulated Darcy's plots and experimental results (Fig. 10). The average value of experimental
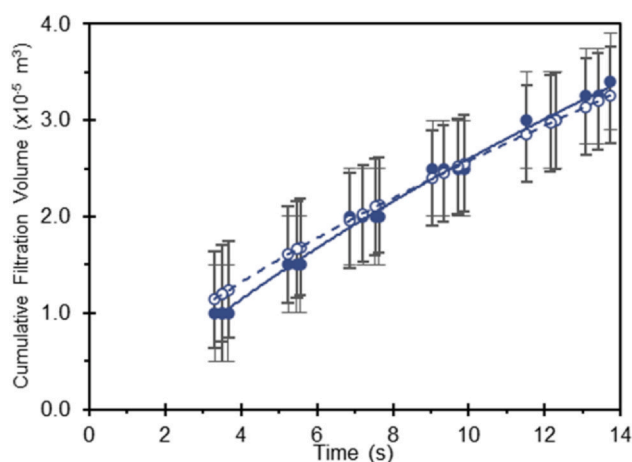
Fig. 10 – Simulated (——●——) and experimental (- -○- -) cumulative filtrate volume over time of the test bed filtration model.

continuous filtration outcomes are compared with the simulation to validate the model (Table S20). In all experiments, *n*-heptane was used as the wash solvent and the filtration and washing driving force was kept to 400 mbar.

The composition of the simulated residual liquid trapped in the solid cake after the successive washes is shown in Table 5. The mother liquor was fully removed from the cake washing and the minimal concentration of MFA in the liquid phase prevents particle agglomeration potentially occurring during drying.

After the second wash, the cake requires deliquoring under vacuum (where the pressure is practically constrained to 400 mbar) to ensure the solvent is removed. A model for airflow deliquoring by suction is based on the volume-average continuity equation proposed by Wakeman and Tarleton, (Tien, 2012; Wakeman, 1979; Wakeman, 1979) predicting cake saturation (S_{cake}), irreducible saturation (S_∞), and residual solvent content (M). Where the cake is saturated with solvent, deliquoring by airflow occurs when the pressure difference imposed exceeds a threshold pressure value (P_b), below which the cake remains saturated (Fig. S20). This can be calculated with consideration of the interfacial tension of the filtrate (σ) and equivalent diameter (d_e) of particles within the cake (Eq. (16)). The Kozney-Carman equation derives a definition of d_e (Eq. (17)).

$$P_b = 4.6(1 - \varepsilon_{av})\sigma/\varepsilon_{av}d_e \tag{16}$$

$$d_e = 13.42\sqrt{\frac{1 - \varepsilon_{av}}{\alpha_{av}\rho_s\varepsilon_{av}^3}} \tag{17}$$

Cake saturation is described as the ratio of the volume of liquid with respect to the volume of cake void. The degree of saturation depends on the pressure difference on the cake that is related to the capillary pressure. The irreducible saturation (Eq. (18)) (Tien, 2012; Wakeman, 1979) denotes solvent trapped within the cake pore space which cannot be removed by airflow deliquoring (blowing or suction), and is related to the capillary number (N_{cap}) (Eq. (19)), where ρ_l is the filtrate density, Δp is the imposed pressure drop of the gas flow and L is the cake thickness. The reduced saturation (S_R) expresses the liquid content of the deliquored cake (Eq. (20)). (Tien, 2012; Wakeman, 1979; Wakeman, 1979)

$$S_\infty = 0.155(1 + 0.031N_{cap}^{-0.49}) \tag{18}$$

$$N_{cap} = \varepsilon_{av}^3 d_e^2 (\rho_l gL + \Delta p)/(1 - \varepsilon_{av})^2 L\sigma \tag{19}$$

$$S_R = S_{cake} - S_\infty/1 - S_\infty \tag{20}$$

GSA identified parameters which would significantly affect deliquoring performance (summarised in Fig. S21). As expected, the moisture mass fraction in the cake decreases with increasing drying time or driving force, as cake saturation/residual moisture mass fraction are affected by particle size and shape, likely due to modified cake porosity.

Table 5 – Simulated test bed washing mass fraction of the composition of the residual solvent left after wash 1 and wash 2.

	Washing					
	Wash 1			Wash 2		
	2-Butanol	MFA	n-Heptane	2-Butanol	MFA	n-Heptane
Simulated	0.1620	0.0025	0.8360	0.0252	0.0040	0.9740

Conversely, a lower driving force results in a high cake saturation as the residual solvent is not effectively displaced. To mitigate effects of high cake resistance in thicker cakes or solvent viscosity where a higher initial amount of residual solvent is present, the driving force must be increased to effectively dry the product. It is noted however that where the solvent has a higher density, applying a higher driving force is shown to have no meaningful effect on residual solvent levels in the cake.

The isolation procedure which will be used for the experimental crystallisation processes will be vacuum filtration under 400 mbar to dryland, followed by two washes using 2 ECVs of n-heptane and deliquoring for 60 s at 400 mbar. The solid will be further dried in a vacuum oven to ensure no residual solvent remains.

6.2. Experimental crystallisation validation

6.2.1. In-line monitoring and sampling considerations for MSMPR experiments

The in-line monitoring techniques utilised during the experimental crystallisation process were UV spectrometry, FBRM, and PVM, which together give information on solute concentration, as well as estimate the number and size of crystals produced. During process operation, samples were taken from the crystallisation vessels for off-line analysis using UV–vis spectrometry and PSD measurements. The target of the final manufacturing process is to produce MFA particles with a D_{90} size of 120 µm.

A method for determination of MFA concentration (X_{MFA}) in ethanol via off-line UV spectrometry was developed for the concentration range 50–300 µg mL^{-1}. The calibration was validated for the presence of up to 1.5% by mass of 2-butanol/n-heptane (90:10 w/w) present in the solution, which is the expected upper limit for the process sampling procedure proposed. The linearity ($R^2 = 0.9997$) and recovery (within 2%) satisfy industrial requirements. (ORA Laboratory Manual Volume II: Methods, 2020)

Partial least squares (PLS) calibration models (see section S5.2.2) to enable prediction of X_{MFA} in 2-butanol/n-heptane (90:10 w/w) by in situ UV spectrometry were constructed using a global approach, in which the model for prediction of concentration also includes variation in temperature. (Chong et al., 2022) Six experiments, each at a different concentration, were carried out to acquire calibration spectra simultaneously for two spectrometer-probe configurations during a cooling programme for each composition (Table S27). The concentration of the solutions was verified via the off-line UV reference method developed for off-line samples. The global concentrations (X_{MFA} = 0.005–0.046) and temperatures (9–74 °C) encompassed by the calibration ensured flexibility with regards to which vessel the in situ UV probes may be deployed. PLS models were constructed independently for the two configurations for prediction of MFA

concentration by UV spectrometry. The performance of Configuration 1 is poorer than Configuration 2 (RMSEP X_{MFA} = 0.0021 and 0.0004 respectively) which may be owing to lower light throughput in Configuration 1. These are within acceptable measurement limits of quantification.

The intended sampling protocol to determine solution concentration throughout the crystallisation process via off-line UV spectrometry was assessed initially using a solution. This was conducted by sampling from a solution of concentration X_{MFA} = 0.009; accounting for inter-operator variability and intended operational temperatures (25–65 °C). Across the off-line UV samples, there was one outlier (Fig. S22). Whilst replicates are necessary to ensure reliable outlier detection, during operation of a multi-stage process replicate samples may not be practically feasible. Omitting the outlier, the mean concentration determined by off-line UV spectrometry over the whole experiment was X_{MFA} = 0.0092 (RSD = 1.8%). For all samples obtained via the proposed sampling protocol, the RMSE of the concentration determined by off-line UV spectrometry was X_{MFA} = 0.0002, which is an error of 2% within the concentration of the solution at preparation. This is within the error margin acceptable for HPLC, (ORA Laboratory Manual Volume II: Methods, 2020) therefore suggesting that off-line UV spectrometry is an appropriate technique for determination of the solution concentration. These values assume consistent solution concentration across the whole experiment, which was unlikely as the final high-temperature (68 °C) sample indicates a slight increase in the concentration during heating (Table S28). Even with inclusion of the outlier the mean concentration for both the low and high temperature samples (mean temperatures of 25 and 66 °C respectively, each set comprising nine samples) was X_{MFA} = 0.0092, with RSDs of 2.9% and 0.3% for the low and high temperature samples respectively. The variability in the concentration determined by this sampling protocol and off-line UV spectrometry is much less than the gravimetric method (Fig. S22) where the mean concentration for three samples was X_{MFA} = 0.0084 (RSD = 14.2%).

6.2.2. One-stage MSMPR

A 1-stage MSMPR experiment was designed with conditions which mimicked the mid-point in a longer, multi-stage cascade (Table 6). The stage temperature was constrained to a maximum temperature of 35.0 °C to allow practical sampling and product collection at a temperature close to the isolation (room) temperature. A start-up concentration in each vessel of ca. 50% into the metastable zone width (MSZW, see section S3.2.4) was selected as a suitable starting point to decrease time to steady state operation, whilst avoiding encrustation and minimising unwanted nucleation. As the process progresses, the supersaturation value within the vessel will change. Due to available equipment, the MSMPR stage was constrained to a 250 mL vessel containing 170 mL slurry. This working volume is based on previous characterisation of the

Table 6 – 1-Stage MSMPR model (and experimental) conditions. *Mean values, measured using laser diffraction without ultrasound.

	Feed	Seed	1	Outlet
		Vessel		
X_{But}	0.8796 (0.8787)	0.8946 (0.8995)		0.8858
X_{MFA}	0.0225 (0.0225)	0.0058 (0.0059)		0.0157
X_{Hept}	0.0978 (0.0988)	0.0944 (0.0946)		0.0985
Liquid phase flow rate (g min^{-1})		0.95		10.91
Solid phase flow rate (g min^{-1})		0.05		0.072
Total flow rate (g min^{-1})	10 (10.2)	1.00 (1.00)		11 (11.2)
Solid phase mean size (μm)		40		
Solid phase st. dev. (μm)		20		
T (°C)	55	20	35.0 (35.0)	35.0
V (mL)			170	
τ (min)			11.8	
X_{MFA} at sat., C^*			0.0135	
X_{MFA}, C_{Cryst}			0.0157	
S_{Cryst}			1.16	
Max S_{Cryst}			1.53	
Liquid mass (g)			128.4	
Solid mass (g)			0.8	
D_{10} (μm)			28.5 (39.1 *)	
D_{50} (μm)			49.5 (76.2 *)	
D_{90} (μm)			85.6 (133 *)	

vessel using computational fluid dynamics (Ojo et al., 2019) to ensure the well mixed conditions assumed by the PBM model. Particles generated during validation of the wet milling model were used as seed material, as the measured particle size ($D_{4,3}$ = 34.1 μm) was consistent with the seed size required to generate particles with D_{90} = 120 μm (Fig. S8). Further, reusing material from earlier experiments reduces the total MFA material required for process development. A start-up procedure was chosen that could be transferred exactly to the intended final 5-stage MSMPR cascade, where the vessel would initially be filled with a saturated solution (X_{MFA} = 0.0135) at the process temperature (35 °C) to minimise the time required to reach steady-state operation.

The 1-stage experiment was carried out with aims to: (1) evaluate start-up procedures for process operation itself and initiate process monitoring equipment; (2) minimise elements of the experiment and process that were not included in the implemented PBM: feed solution or slurry variation, tube blockages, encrustation, *etc.*; (3) assess variability in slurry sampling for off-line analysis (particle sizing and solute concentration of the liquid phase); (4) isolate solid and liquid to enable mass balance loop closure (solid mass, solute concentration of the liquid phase); and (5) verify model predictions for model parameter testing and verification. The modelled conditions for the 1-stage MSMPR experiment are collated in Table 6, and the process will be deemed successful if the steady-state solution concentration and particle size measurements fit within the design space predicted by the crystallisation model.

The process was operated for 2.5 h with slurry sampling carried out every 30 min (2 residence times). No encrustation was observed in the vessel or fouling on the PAT probes.

For each timepoint, four samples were taken for the purposes of measuring the solute concentration of the solution phase off-line, determining the mass balance, measuring the

solute concentration of the solution phase off-line and off-line particle sizing.

The MFA concentration of the feed solution, determined off-line using UV spectrometry was X_{MFA} = 0.0228, 1.2% greater than the concentration from the feed preparation. The off-line MFA concentration for ten samples taken from the vessel during the process (two each at five timepoints, Table S30) was constant; the mean value was X_{MFA} = 0.0166 (RSD = 0.8%). For each set of samples, the replicate differences are generally low, varying between 0.2% and 2.1%. The concentration determined *via* off-line UV spectrometry exceeds the expected concentrations generated both from the initial PBM (X_{MFA} = 0.0157) and after the operating parameters were updated with the experimentally determined parameters to further improve the model (X_{MFA} = 0.0155).

The UV attenuated total reflectance (ATR) probe in Configuration 2 (see section S5.2.2) was present during the 1-stage MSMPR experiment. To maintain sampling port access, the addition of a second probe in Configuration 1 was not practically feasible. The mean MFA concentration determined through *in situ* monitoring was X_{MFA} = 0.0171 (RSD = 0.4%), a deviation of X_{MFA} = 0.0005 from the value determined off-line. There is in general good agreement between the *in situ* and off-line MFA concentrations determined. Additionally, for the *in situ* concentration, there are spikes of higher concentration corresponding to periods of sampling. This may be attributed to the decrease in volume from removal of a sample (*ca.* 20–30 mL) for particle sizing and the ATR probe no longer being sufficiently submerged (Fig. S25).

Particle size measurements of samples taken from the crystalliser vessel in the 1-stage MSMPR experiment are listed in Table 6. A measured D_{90} value of 133 μm is considerably higher than the predicted value of 85.6 μm, and this value reduces slightly to 107 μm on the application of ultrasound (Table S33). Discrepancies in the model and

		Vessel			
	Feed	**Seed**	**1**	**2**	**Outlet**
X_{But}	0.8746 (0.8746)	0.8948 (0.8895)			0.8832
X_{MFA}	0.0282 (0.0282)	0.0058 (0.0059)			0.0186
X_{Hept}	0.0972 (0.0972)	0.0944 (0.0946)			0.0982
Liquid phase flow rate (g min^{-1})		0.95			10.87
Solid phase flow rate (g min^{-1})		0.05			0.14
Total flow rate (g min^{-1})	10 (10.0)	1.00 (1.00)			11.00 (11.00)
Solid phase mean size (µm)		40			
Solid phase st. dev. (µm)		20			
T (°C)	65	20	39.0 (39.0)	33.0 (33.0)	33.0
V (mL)			170	170	
τ (min)			11.7	11.8	
X_{MFA} at sat., C^*			0.0167	0.0120	
X_{MFA}, C_{Cryst}			0.0186	0.0133	
S_{Cryst}			1.11	1.10	
Max S_{Cryst}			1.53	1.54	
Liquid mass (g)			127.5	127.9	
Solid mass (g)			1.6	2.3	
D_{10} (µm)			31.5	35.4 (51.9 *)	
D_{50} (µm)			58.2	64.5 (97.5 *)	
D_{90} (µm)			109	118 (168 *)	

Table 7 – 2-Stage MSMPR model (and experimental) conditions. *Measured using laser diffraction without ultrasound.

experimental particle sizes were attributed to the temperature of the stage being higher than room temperature; resulting in significant de-supersaturation whilst preparing for the off-line PSD measurement creating fine particles on the surface of the MFA crystals. Overall, as no practical issues were encountered during operation of this 1-stage experiment, development progressed to a multi-stage cascade.

6.2.3. Two-stage MSMPR

Following the 1-stage mid-point mimic experiment, a 2-stage experiment was designed. The addition of multiple crystalliser stages introduces slurry transfer lines between crystallising stages which are susceptible to blockages, and the primary purpose of this 2-stage MSMPR experiment was to practically evaluate options to minimise blockage occurrences and test mitigation strategies in preparation for a 5-stage MSMPR manufacturing process. The constraint of a final product stream temperature between 20 and 35 °C was imposed to ensure practically feasible sampling and mimic later production stages where high slurry loads increase fouling and blockage probability. Alongside this, minimising variability in feed solution and slurry concentrations was investigated.

This 2-stage experiment was designed using the conditions adopted in the 1-stage experiment (Table 7), increasing the total experiment duration to 5 h to allow time for possible challenges to arise (2.5 h in 1-stage). An increased feed vessel jacket temperature of 65 °C (60 °C in 1-stage) was used to better mimic the temperature points within a longer MSMPR cascade. The agitation rate was increased (from 250 rpm to a target minimum of 400 rpm) to ensure the well-mixed homogeneous particle suspension assumed by the crystallisation model. A contingency would also be regular cleaning of the inter-vessel transfer lines.

The crystallisation process was successfully operated over 4 h at steady state (10τ). The increased agitation rate, to 400 rpm, improved suspension of the solid in the vessels and prevented the formation of large agglomerates. Further, the frequent transfer line cleanings (every 15–30 min) ensured no major blockages were observed during the run.

Consistent with the sampling protocol for the 1-stage experiment, slurry samples were taken from both MSMPR stages during the process. The mean concentrations determined for Stage 1 were $X_{MFA} = 0.0177$ (off-line, RSD = 1.0%) and $X_{MFA} = 0.0183$ (in situ, RSD = 1.2%) and for Stage 2 were $X_{MFA} = 0.0134$ (off-line, RSD = 1.8%) and $X_{MFA} = 0.0132$ (in situ, RSD = 2.2%). There were some signs of fouling on the UV probes post-process (Fig. S29), however no deposition of material on the ATR crystal measurement surfaces was identified. Additionally, the shape of the UV spectra obtained was comparable to the calibration spectra and the agreement of the concentration values determined via in situ measurements with the off-line measurements indicates that the fouling was not detrimental in this instance.

Like in the 1-stage MSMPR experiment, the MFA particle size D_{90} within the stage sampled is higher than the predicted value (model: 118 µm, experimental: 168 µm). A minor reduction in size to 145 µm was observed when the PSD was measured with ultrasound (Table S37), which is suggestive of some particle agglomeration, but was not considered significant. Overall, the 2-stage experiment was deemed successful, and confirmed readiness to progress to a full 5-stage manufacturing process.

6.3. Manufacture of $D_{90} = 120\,µm$ particles

6.3.1. Five-stage MSMPR

Following successful model validation on the 2-stage MSMPR experiment and with a fully developed isolation procedure developed, an MFA manufacturing run in a 5-stage MSMPR crystallisation was carried out. In combination with the PBM, a range of attainable sizes calculation (Section 4.3.4) indicated that this platform under seeded conditions would deliver high quality MFA particles with a D_{90} of 120 µm using the digitally designed crystallisation and isolation processes. The number of particles present in stages 2, 3 and 5 of the 5-stage cascade were monitored by in situ FBRM, and in stage 3

Table 8 – Model proposed (and experimental) steady state conditions for 5-stage crystallisation experiment. *Measured using laser diffraction without ultrasound.

| | Feed | Seed | Vessel | | | | | Outlet |
			1	2	3	4	5	
X_{But}	0.8622 (0.8622)	0.8948 (0.8276)						0.8924
X_{MFA}	0.0420 (0.0420)	0.0058 (0.0805)						0.0085
X_{Hept}	0.0958 (0.0958)	0.0944 (0.0920)						0.0992
Liquid phase flow rate (g min^{-1})		0.96						12.14
Solid phase flow rate (g min^{-1})		0.04						0.43
Total flow rate (g min^{-1})	11.57 (11.57)	1.00 (1.01)						12.57
Solid phase mean size (μm)		27.2						
Solid phase st. dev. (μm)		11.8						
T (°C)	75	20	51.0 (51.6)	43.3 (44.0)	36.5 (36.9)	30.5 (31.1)	25 (25.9)	25
V (mL)			170	170	170	170	170	
t (min)			10.2	10.3	10.4	10.4	10.5	
X_{MFA} at sat., C^*			0.0295	0.0208	0.0146	0.0104	0.0076	
X_{MFA}, C_{Cryst}			0.0322	0.0232	0.0163	0.0117	0.0085	
S_{Cryst}			1.09	1.11	1.12	1.12	1.12	
Max S_{Cryst}			1.30	1.54	1.57	1.56	1.53	
Liquid mass (g)			126.3	126.5	126.8	127.2	127.7	
Solid mass (g)			1.3	2.5	3.4	4.1	4.5	
D_{10} (μm)			23.9	29.6	32.7	34.5 (51.9 *)	35.6 (57.3 *)	
D_{50} (μm)			44.4	54.4	59.1	61.8 (134 *)	63.3 (137 *)	
D_{90} (μm)			84.7	101.2	108.0	111.7 (291 *)	113.8 (274 *)	
$D_{(4,3)}$ (μm)			50.3	61.0	65.9	68.6	70.2	

images of the particles were captured by PVM. The in-line concentration of MFA was measured in stages 2 and 5. The 5-stage continuous crystallisation (Fig. S32) was operated according to the conditions prescribed by the model (Table 8). Consistent with the previous 1- and 2-stage experiments, the process commenced with saturated solutions present in all 5 vessels. Based on prior MSMPR operations, steady state was predicted to be achieved in vessel 5 after *ca.* 2 h. For an expected solid MFA throughput of 26.2 g h^{-1} (Table 8), operating at steady state for 4 h should produce 104.9 g of product material.

The total FBRM counts for the targeted size range (100–300 μm) was observed in real-time to have plateaued in the measured stages (2, 3 and 5) after 120 min, implying steady state had been reached (Fig. S34) and product collection began at the outlet of stage 5. Overall, the process ran at this steady state for 3.6 h, with minimal operator intervention and no major transfer line blockages. Periodic cleaning of the overflow and transfer lines allowed any large particles to be cleared before significant obstructions occurred. There was rapid fouling of both UV ATR probes during the experiment, evidenced by a drifting baseline and the shape of the spectra drastically changing with experiment progress. Therefore, *in situ* concentration monitoring was unsuccessful in this instance. This contrasts with the inconsequential fouling observed in the 1-stage and 2-stage experiments.

The slurry sampling protocol (sections S5.3.1 and S5.3.2) was used to take samples during the process. The concentration of the feed solution determined *via* off-line UV spectrometry was X_{MFA} = 0.0423, a good agreement between the off-line UV spectrometry technique and expected concentration from the feed solution preparation. Across the experiment, the highest RSD in the concentration determined for each stage *via* off-line UV spectrometry was 1.6% (Table 9). This consistency in the determined solution concentration confirms that the process was operating at steady state and there was little variance in the samples. During production PVM images indicated aggregates were

Table 9 – Mean and RSD of the solution concentration determined *via* off-line UV spectrometry for each stage in the 5-stage experiment.

| | Stage | | | | |
	1	2	3	4	5
Modelled X_{MFA}	0.0295	0.0208	0.0146	0.0104	0.0076
Mean Exp X_{MFA}	0.0296	0.0212	0.0155	0.0120	0.0095
RSD (%)	0.9	1.6	1.0	1.3	1.1

forming in stage 3, and the PSD of slurry samples taken from this stage are consistent with this (Table S41). Applying ultrasound during the measurement resulted in a reduction in particle size, indicating these aggregates were loosely held together.

The suspension exiting the final MSMPR vessel was collected and isolated using the filtration, washing and deliquoring protocols developed. The crystallised suspension had a solid load of approximately 3.5 w%, which is consistent with the predicted value (predicted outflows: 12.14 g min^{-1} liquid; 0.43 g min^{-1} solid; solid load 3.48 w%), but is considerably lower than the typical > 10 w% used in isolation procedures. (Ottoboni et al., 2020; Perlmutter, 2015) To increase suspension loading and reduce isolation process time, the crystallised suspension was concentrated by partial removal of the liquid phase (see section S5.3.1). From each initial 250 mL product suspension batch (12 total), a concentrated 50 mL suspension aliquot was isolated with a mean solid load of 24.5 wt% (Table S42). The concentrated suspension was filtered to breakthrough using a vacuum of 400 mbar; the mean filtration flow rate corresponded to 2.52 mL s^{-1} and the mean filtered cake volume obtained was 14.05 mL, with a cake resistance of 9.98×10^7 m kg^{-1}. The filtered cake was then washed twice using 2 ECVs of *n*-heptane to remove any residual mother liquor and prevent any particle agglomeration during drying. The cake was deliquored for 60 s at 400 mbar. The washed cake was dried at 40 °C (50
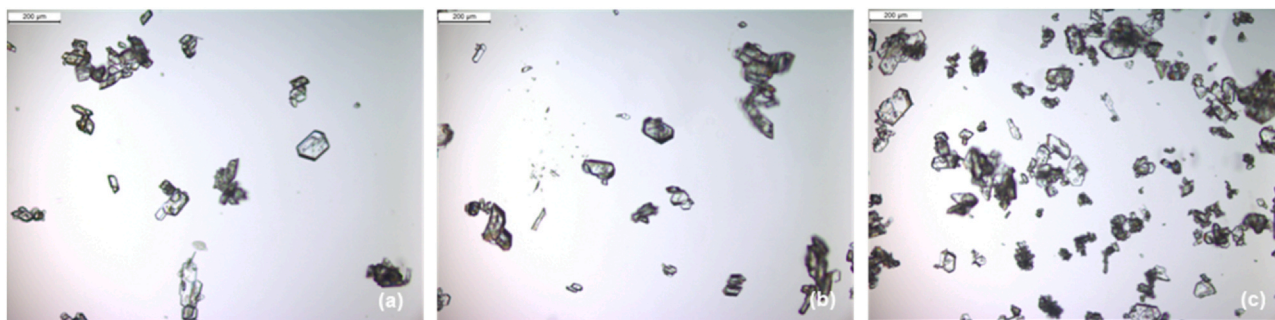
Fig. 11 – Optical microscopy images of (a) sample S5 from the 1-stage MSMPR experiment; (b) sample S4 from the 2-stage MSMPR experiment; and (c) the blended product batch from the 5-stage MSMPR experiment.

mbar) and was determined dry once the mass was consistent over 3 consecutive days. This vacuum drying reduced the mass of the deliquored material from 77.0 g to 71.2 g. The mean loss on drying, wet basis, achieved corresponded to 11.0% (standard deviation = 0.57%). Comparison of the mean particle size D_{90} in the slurry samples taken during the process with the isolated product particles in the dried cakes (Table S41 and Table S44) suggests that the isolation procedure broke up some loosely bound aggregates. The isolated D_{90} particle size is 16% smaller than the slurry particle size using the same measurement technique (235 μm and 274 μm, respectively).

Product was collected from the crystallisation process for 216 min (3.6 h), and according to the model this should result in 94.5 g of solid MFA particles in the product suspension. Considering slurry samples were removed from Stages 4 and 5, and product outlet stream was collected for a total of 16 min for sampling, this expected mass value reduces to 82.4 g. Given 71.2 g of dry MFA was isolated, this results in a product recovery value of 91.2% (Eq. (21)). Some mass loss can be expected from periodic cleaning of the inter-vessel transfer lines and slurry transfers during the isolation process.

$$Product\ \ recovery = \frac{mass\ \ isolated}{mass\ \ expected} \cdot 100 \tag{21}$$

Although the in-line FBRM measurements had indicated that steady state had been reached before product slurry collection was started, particle size measurements across the 12 sequential product batches (Table S44, each aliquot equals *ca.* 18 min of product collection) suggests this is not the case. Further, aliquot 1 did not conform to LOD standards (Table S43). It is not until aliquot 3 that the product batch particle sizes and LOD conformance become consistent. Therefore, the final product blend was limited to aliquots 5–11, and batches 1–4 were discarded. This post-process analysis approximates steady state as in reality being reached after 192 min (3.8τ) of process operation. The combined mass of the blended sample was 50.6 g, and this was further analysed to ensure compliance with pharmacopoeia requirements (Mefenamic Acid Specification, 2023) for polymorph (form I, Fig. S38) and LOD (0.08%, Table S43).

The particle size D_{90} of the blended powder (236 μm) is consistent with the mean value measured across the original 12 aliquots under the same measurement conditions (235 μm). The D_{90} size of the blended powder varies depending on the method of measurement, 236 μm for laser diffraction and 186 μm for optical microscopy techniques (Table S45), as do the PSD spans (1.84 and 1.30 respectively). We reason that this is due to agglomeration of the particles,

and that during powder dispersion these are broken up, resulting in a lower D_{90} value. This is supported by an observed stepwise decrease in D_{90} size to 178 μm and 128 μm when medium and high dispersion energies are respectively applied to powder samples (Table S45). Applying ultrasound during the slurry measurement decreased the mean measured D_{90} size from 236 μm to 169 μm, further evidence for the agglomerate formation. Comparing images captured of the bulk and dispersed powder (Fig. S39 and Fig. S40), we conclude that the 5-stage MSMPR crystallisation yielded primary particles with the targeted D_{90} size (model: 120 μm, experimental: 128 μm), however these are weakly bound together into agglomerates with a particle size of 236 μm.

During the PBM estimation and validation experiments agglomeration was not observed, and comparison of D_{90} sizes measured with and without ultrasound indicated that little agglomeration occurred during the 1-stage and 2-stage MSMPR crystallisations (Table S32 and Table S37). Therefore, terms which capture the kinetic processes involved in particle agglomeration were not included within the model used to design the manufacturing process. However, on further inspection, microscopy images of samples taken during the development experiments indicate some agglomeration is present (Fig. 11). To improve the accuracy of the PBM model, we undertook the retrospective estimation and validation of appropriate agglomeration terms, for comparison with the experimental 5-stage MSMPR manufacturing run.

6.3.2. Addition of agglomeration kinetics

Agglomeration occurs when two or more crystals collide during the crystal growth and there is sufficient contact time for a bridge between them to form. (Pérez-Calvo et al., 2016; Bari and Pandit, 2018) In the case of reduced contact time, then weak bonding will result and no agglomerates will form. Hence, the agglomeration rate depends on the particle collision rate, and is related to colliding particle sizes and the probability.

The modelled agglomeration efficiency A_g is based on the Mumtaz number A_{50}, describing the strength of the crystalline bridge binding the agglomerate. (Pérez-Calvo et al., 2016; Hounslow et al., 2001; Pitt et al., 2012) As solution supersaturation is depleted, the crystal tends to grow, as does the strong interaction between the solute and solvent molecules. Considering that the initial contact between the two colliding particles lies along a line, the agglomeration model is defined by Eq. (22).

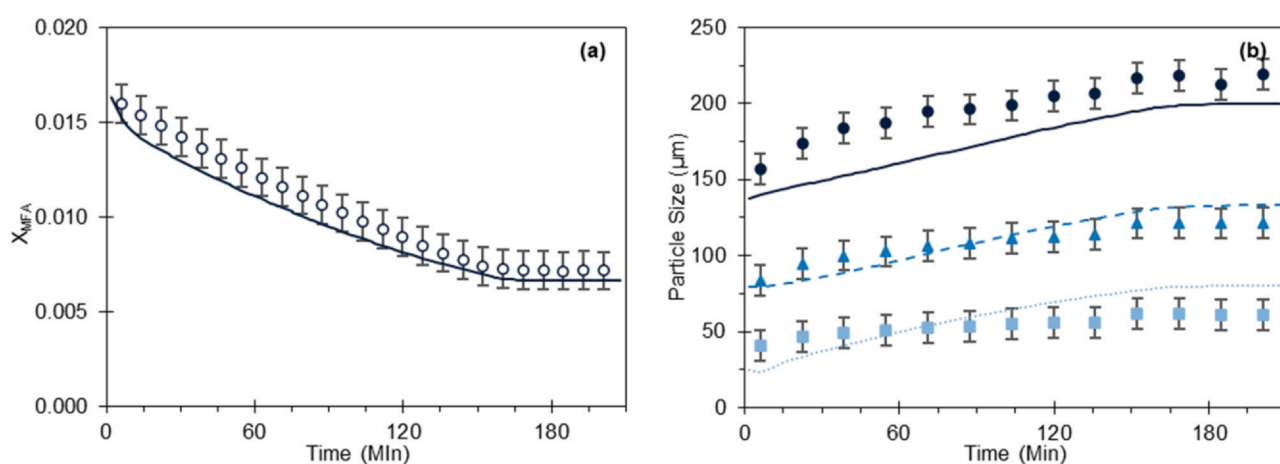$$A_g = \frac{A_{50}G}{\mu d^2 \gamma^2} \Big/ 1 + \frac{A_{50}G}{\mu d^2 \gamma^2} \tag{22}$$

Fig. 12 – (a) Comparison of (○) experimental (measured _in situ_) and (—) predicted X_{MFA} during the batch crystallisation to determine agglomeration kinetics. (b) Comparison of experimental (points, measured _in situ_) and predicted (lines) particle size (■; ⋯) D_{10}, (▲; ▲) D_{50}, (●; —) D_{90} during the batch crystallisation to determine agglomeration kinetics.

Two further batch experiments were performed to obtain the agglomeration kinetic parameters, with MFA saturation temperatures of 30 and 35 °C (Table S46). A slow linear cooling profile was applied and 20 w% of milled seeds were added. The seed material was generated using an _in situ_ milling device, (This work was carried out at separate research sites) and in general had a wide PSD span and contained a high proportion of fines. The simulated and experimental decrease in MFA solution concentration are in good agreement (Fig. 12a), indicating the model accurately simulates crystallisation. The measured particle sizes (D_{10}, D_{50} and D_{90}) also agree well with the predicted values (Fig. 12b), with D_{50} being the most accurately predicted.

From these batch experiments, the agglomeration efficiency parameter A_{50} is estimated as 0.01 (standard deviation = 0.059). This aligns with the 95% confidence interval on the deviation from D_{10} and D_{90}. The particle size measurements across the two experiments with the same operating conditions were consistent, indicating good reproducibility across the agglomeration experiments.

The A_{50} was added into the PBM and the 5-stage process was re-modelled within gFP, implementing the experimental parameters listed in Table 8. Under these conditions, the improved PBM predicts a D_{90} in stage 5 of 336 µm (Table 10), more consistent with our experimental agglomerated D_{90} size of 274 µm. The isolation procedure then breaks up some of the agglomerates to reduce the D_{90} size of blended powder to 236 µm.

The agglomeration observed will not impact the product performance assessment in this work. The compression forces exerted on the particles during tableting will be much higher than the dispersion forces used during PSD measurement. Therefore, the agglomerates will be broken up into their primary particles (D_{90} = 128 µm), which are within the design space of the modelled D_{90} size.

7. Performance testing

7.1. Dissolution testing conditions

The rationale for the choice of dissolution medium aimed to provide a more biorelevant approach rather than using the pharmacopeial quality test method employing a 0.05 M tris dissolution buffer pH 9 containing 1% sodium dodecyl sulfate. The standard biorelevant dissolution medium fasted simulated intestinal fluid (Fassif) is a phosphate buffer with a pH of 6.5, also containing sodium chloride, phospholipis (lecithin) and bile salt (taurocholate). (Bou-Chacra et al., 2017)

As a weak acid (pK_a = 4.2), MFA solubility is highly pH dependent. A recent study depicted MFA solubility _vs_ pH in biorelevant media. (Abuhassan et al., 2022) The solubility of MFA at pH 6.5 was very low and this pH may therefore not be suitable for MFA dissolution assay (since a high dose of 250 mg is investigated and UV detection may be difficult at low concentrations). Khadra _et al._ (Khadra et al., 2015) investigated the impact of buffer composition of biorelevant media on solubility of acidic, basic and neutral drugs, showing that the solubility of acids was predominantly impacted by pH rather than ingredients such as bile salts and phospholipids.

7.1.1. Impact of buffer pH on UV analysis

The rationale for the choice of dissolution medium was therefore a 'blank' Fassif medium, lacking bile salts and phospholids, since the presence of these ingredients does not significantly impact solubility of MFA and to reduce costs as bile salts are expensive. MFA precipitation was observed for all dilutions (50–200 µg mL^{-1}) at pH 6.5. At pH 7.0, precipitation was observed at concentrations from 100 to 200 µg mL^{-1}. At pH 7.4 the widest range of MFA remained in solution with only precipitation being detected at 200 and 300 µg mL^{-1}.

7.2. Experimental dissolution testing

The dissolution profile was used to measure particle performance and was modelled using the Human GI tract model in

Table 10 – Model proposed (and experimental) steady state conditions for 5-stage crystallisation experiment. *Mean value, measured using laser diffraction without ultrasound.

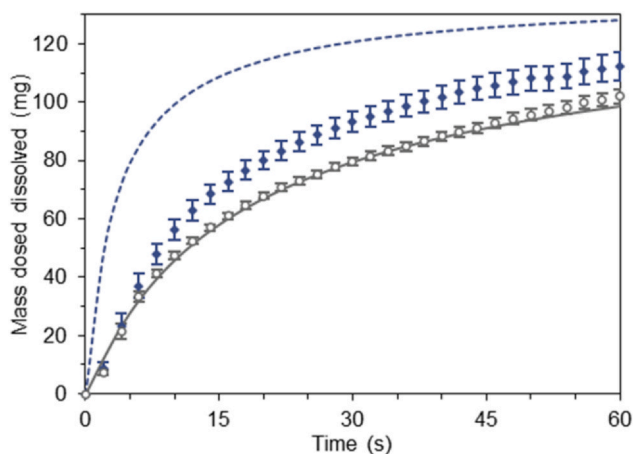|			Vessel			Product
	1	2	3	4	5	
D_{10}	32.4	61.0	85.2	103 (51.9*)	114 (57.3*)	(37.8*)
D_{50}	76.2	130	168	194 (134*)	209 (137*)	(108*)
D_{90}	148	234	285	317 (291*)	336 (274*)	(236*)

Fig. 13 – Performance testing of MFA particular products.
(◆) D_{90} = 42 µm, experimental; (- -) D_{90} = 42 µm, predicted;
(○) D_{90} = 120 µm, experimental; (——) D_{90} = 120 µm, predicted.

gFP. The dissolution model differs from the pharmacopeial dissolution testing, in that the model is based on drug dissolution in physiologically relevant media. The predicted dissolution of MFA particles in 'blank' Fassif pH 7.4 was faster in the case of the smaller particles compared to the larger particles. This agreed with experimental results, where the smaller particles reached their solubility limit of 120 mg mL^{-1} at 75 min, faster compared to the larger particles (105 min). Whilst the prediction of the larger particles was in good agreement with the *in vitro* dissolution model (f_1 = 1.7; f_2 = 85.3), a larger discrepancy (Fig. 13) was observed for the smaller particles (f_1 = 25.4; f_2 = 25.7). Exact reasons for the poor fit between predicted and measured dissolution of these smaller particle sizes is unclear. A sizable difference in the dissolution curves was predicted for the two different particle sizes (f_1 = 35.8; f_2 = 19.1). Whilst more MFA dissolved using the smaller particle material, the difference was not significant. After 45 min the mass of MFA dissolved was similar (D_{90} = 42 µm, 104.04 mg dissolved; D_{90} = 120 µm, 90.5 mg dissolved) and experimentally the two products had reasonably similar profiles (f_1 = 13.0; f_2 = 46.8).

8. General remarks

Increasing numbers of small organic molecules with high potency (and low dosages) are gaining new medicine approvals. (Brown and Wobst, 2021; De, 2023; Bartlett, 2023) Between 1999 and 2015 the number of new chemical entities (NCEs) requiring large volume production of more than 10 mega tonnes per year fell by 75%. (Moorcroft et al., 2023) Ensuring material usage during development does not outweigh production volumes is crucial. Implementation of digital design approaches promises to reduce the amount of material required in process development. Controlling particle size has been identified as one of the most material-intensive targets in the development of a pharmaceutical crystallisation, (Harris and Matthey) and continuous processes typically accrue more material loss during development than batch processes through startup procedures. (Zhang et al., 2017) Overall, 1513 g of API was used in this work across the parameterisation and validation of seven models, as well as production runs for two particle sizes (Table S51 depicts a detailed breakdown). From this 90 g of

material with a D_{90} of 42 µm was produced and 71.2 g of material with a D_{90} of 120 µm was produced. The 5-stage MSMPR process yielded 71.2 g MFA in 216 min, which can be extrapolated to 474 g per 24 h at steady state, equating to 1898 doses of 250 mg. When compared with our previously reported seeded cooling crystallisation workflow procedure which used 10 kg of API throughout development, (Brown et al., 2018) the incorporation of digital design tools resulted in a reduction of an order of magnitude in material usage whilst developing two separate processes. Further, throughout the development process, material saving activities reduced the resource requirements. Some experiments were eliminated from the development process and others were streamlined. Whilst it is difficult to determine how many experiments would have been required for a traditional development approach, examples of reducing experimentation include using an initial *in silico* solvent screen removed the need for extensive solubility experiments leading to a limited candidate screen, and GI tract modelling removed most initial dissolution experiments from target setting activities. Using a single batch of MFA for multiple parameterisation experiments when building the PBM, re-purposing material produced in wet milling parameterisation experiments as seeds for the cooling crystallisations, and iterative filtration techniques to parameterise isolation models also reduced material requirements throughout development.

The process understanding of MFA crystallisation achieved through our digital-first approach is transferrable to other particle size quality targets for this model system. When applying a similar approach to an active end-to-end drug development process, where CQAs are liable to change, in theory no additional experimentation would be required outside of process demonstration should a different particle size be targeted. This study targeted product with specific D_{90} sizes, however as the full particle size distribution is considered in the developed models, processes targeting other quantiles (*e.g.*, D_{10} or D_{50}) could also be designed without further experimental validation.

Accurate characterisation of the PSD of the MFA products obtained was critical to assess the product quality and determine process success. However, inconsistencies across different PSD measurement methods of the same product batch were observed, which highlighted the presence of weakly bound agglomerates and steered us towards improving the PBM by including an agglomeration term. This highlights the need for cross-platform characterisation to fully characterise a solid product.

In demonstrating the application of these models to process design, gaps or weaknesses in current modelling approaches have been identified. Two related themes emerge: model specificity and unmodelled physical phenomena. The mathematical models for process design are highly specific for the product attribute targeted, in this case the particle size D_{90} measurement. In isolation development it was noted that current filtration and washing models do not include impurity concentration terms, and so do not predict the removal of impurities during this operation. Incorporation of this into future model development will be integral to robust digital process design to fulfil multiple product quality attribute specifications simultaneously.

The dissolution profile of the smaller particle size product was significantly overestimated in predictions, and we hypothesise that the underlying cause is related to the

measurement of the particle size and/or the increased surface area in relation to particle volume. It is difficult to accurately determine the size of small particles, and any errors in measurement will amplify the discrepancy in fit as the model uses the cubic radius of the particle size. Further, small particles have a greater surface area, and the wettability of the material may be influential on the dissolution profile, however this parameter is not included in the predictive dissolution model. To alleviate the challenges associated with model specificity, multi-objective models need to be developed, where more than one CQA can be targeted simultaneously.

Aside from the model specificity affecting other product attributes and performance, unmodelled phenomena can directly impact the process. We were unable to move directly from a 1-stage to a 5-stage MSMPR cascade for the seeded cooling crystallisation process, as this introduces transfer lines between vessels. The flow of suspension in these lines is not modelled, and therefore possible blockage mitigation protocols needed to be empirically screened before attempting a production run. Currently, this phenomenon is system dependent and cannot be predicted, leading to inevitable experimental screening. Moving forwards, increasing model capability to include transfer lines and their associated challenges would further decrease the experimentation required to develop a continuous crystallisation process.

9. Conclusion

This work illustrates the state-of-the-art in a digital-first approach to pharmaceutical process development using first principles mathematical models. Detailed mechanistic understanding facilitated the engineering of high-quality MFA particles for specific product performance outcomes, with consideration of the wider end-to-end manufacturing process. The holistic approach is demonstrated over several unit operations in series; selection of quality targets, screening solvents and crystallisation modes, wet milling for a smaller particle size, cooling seeded crystallisation for a larger particle size with accompanying isolation procedure and testing product performance through dissolution. Using efficient experimental planning the material requirement for model parameterisation was effectively minimised, and overall, 1513 g of MFA was used to develop the process across the included unit operations. Using GSA, the ideal conditions for wet milling and a 5-stage MSMPR cascade crystallisation were determined and two products with distinctly different particle sizes were delivered, with D_{90} values of 49 μm and 128 μm. The process understanding achieved in this study would allow future MFA manufacturing processes to be designed digitally which target other particle sizes of any quantile without further experimentation.

Identified challenges in the crystallisation process were related to unmodelled phenomena highlighting gaps in first-principles models where data-driven approaches could be applied in future. When applied to the MSMPR cascades, the PBM is highly specific at modelling crystallisation phenomena within the well-mixed vessels but does not model the transfer lines which link them together. As a direct consequence, a 2-stage MSMPR experiment was required, using experience-driven empirical knowledge to determine whether blockages within transfer lines were likely within the final manufacturing process. This emphasises the need to include "practical running" metrics into the multi-

objective optimisation of the crystallisation where phenomena are not included in the models. The dissolution performance of the smaller particle size product was not as anticipated, with a lower dissolution rate postulated to be due to either errors in particle size measurement or reduced particle wettability, a parameter not included in the model used in the property prediction.

At the current capability of digital process design, practical experiments are still required for pharmaceutical process development. Every API system has material properties and rate processes which cannot (at present) be predicted. Experimental evaluation is needed to identify such processes, develop ways to minimise them, include them in the multi-objective criteria for process operating conditions selection and set process operating limits to avoid or minimise them. Moving forwards, we will address the weaknesses identified to further digitise process design and enable a true "Quality by Digital Design" approach to pharmaceutical manufacturing.

CRediT authorship contribution statement

SJU: Investigation – Solvent selection for crystallisation experiments; Visualization – Overall project; Writing – original draft, review and editing (Lead). **MWSC**: Methodology/Investigation – Large particle size experiments/PAT; Writing – original draft. **WL**: Methodology/Investigation – Population balance model; Writing - original draft. **JMcG**: Methodology/Investigation – Large particle size experiments. **BM**: Methodology/Investigation – Small particle size model, Writing -original draft. **SO**: Methodology/Investigation – Isolation model and experiments, wash solvent selection; Writing -original draft. **MP**: Methodology/Investigation – Small and large particle size experiments. **EP**: Methodology/Investigation – Product performance; Writing -original draft. **MR**: Methodology/Investigation – Solvent selection for crystallisation model; Data curation – Overall project. **MMcG**: Investigation – Small particle size experiments. **MaA**: Investigation – Isolation. **EG**: Investigation – Isolation. **MS**: Investigation – Isolation. **IH**: Project management/administration – Technical and Process development. **HF**: Project management/administration. **BB**: Funding acquisition; Supervision – Population balance model. **CJB**: Funding acquisition; Supervision – Overall project; Methodology/Investigation – Upstream and process considerations, quality target selection; Writing - original draft. **GWH**: Funding acquisition; Supervision – Product performance. **BJ**: Funding acquisition; Supervision – Solvent selection for crystallisation. **AN**: Funding acquisition; Supervision – Large particle size experiments/PAT. **CJP**: Funding acquisition; Supervision – Isolation model and experiments. **CDR**: Funding acquisition; Supervision – Population balance model. **JS**: Funding acquisition; Supervision – Large particle size experiments. **AJF**: Conceptualization/Supervision/Funding acquisition - Overall project. **All authors** contributed to final editing and have approved the final version of the manuscript.

Data Availability

Comprehensive details of experimental materials and methods can be found in the accompanying Supplementary Information. All data underpinning this publication are

openly available from the University of Strathclyde KnowledgeBase at https://doi.org/10.15129/af47190f-2f89–476b-bdbe-0d567f6da3b9.

Declaration of Competing Interest

Acknowledgements

Appendix A. Supporting information

Supplementary data associated with this article can be found in the online version at doi:10.1016/j.cherd.2023.07.003.

References

Abuhassan, Q., Khadra, I., Pyper, K., Augustijns, P., Brouwers, J., Halbert, G.W., 2022. Fasted intestinal solubility limits and distributions applied to the biopharmaceutics and developability classification systems. Eur. J. Pharm. Biopharm. 170, 160–169.

Agimelen, O.S., Jawor-Baczynska, A., McGinty, J., Dziewierz, J., Tachtatzis, C., Cleary, A., Haley, I., Michie, C., Andonovic, I., Sefcik, J., Mulholland, A.J., 2016. Integration of in situ imaging and chord length distribution measurements for estimation of particle size and shape. Chem. Eng. Sci. 144, 87–100.

Agimelen, O.S., Svoboda, V., Ahmed, B., Cardona, J., Dziewierz, J., Brown, C.J., McGlone, T., Cleary, A., Tachtatzis, C., Michie, C., Florence, A.J., Andonovic, I., Mulholland, A.J., Sefcik, J., 2018. Multi-sensor inline measurements of crystal size and shape distributions during high shear wet milling of crystal slurries. Adv. Powder Technol. 29, 2987–2995.

Ahmed, B., Brown, C.J., McGlone, T., Bowering, D.L., Sefcik, J., Florence, A.J., 2019. Engineering of acetaminophen particle attributes using a wet milling crystallisation platform. Int. J. Pharm. 554, 201–211.

Andreassen, J.P., Hounslow, M.J., 2004. Growth and aggregation of vaterite in seeded-batch experiments. AIChE J. 50, 2772–2782.

Austin, L., Shoji, K., Bhatia, V., Jindal, V., Savage, K., Klimpel, R., 1976. Some results on the description of size reduction as a rate process in various mills. Ind. Eng. Chem. Process Des. Dev. 15, 187–196.

Bari, A.H., Pandit, A.B., 2014. Ultrasound-facilitated particle breakage: estimation of kinetic parameters using population balance modelling. Can. J. Chem. Eng. 92, 2046–2052.

Bari, A.H., Pandit, A.B., 2018. Sequential crystallization parameter estimation method for determination of nucleation, growth, breakage, and agglomeration kinetics. Ind. Eng. Chem. Res. 57, 1370–1379.

Bari, A.H., Chawla, A., Pandit, A.B., 2017. Sono-crystallization kinetics of K2SO4: estimation of nucleation, growth, breakage and agglomeration kinetics. Ultrason. Sonochem. 35, 196–203.

L. Bartlett, The Grand Promise of Small Molecules, https://kvalito.ch/the-grand-promise-of-small-molecules/, (accessed 15 May 2023).

BASF SE, ZoomLab, https://myapps.basf.com/ZoomLab/Login, (accessed 1 September 2021).

BIOVIA, Dassault Systèmes, BIOVIA COSMOtherm, Release C30_1705; BIOVIA Pipeline Pilot, Release 2020, San Diego: Dassault Systèmes, 2019.

Black, S., Muller, F., 2010. On the effect of temperature on aqueous solubility of organic solids. Org. Process Res. Dev. 14, 661–665.

Boobier, S., Hose, D.R.J., Blacker, A.J., Nguyen, B.N., 2020. Machine learning with physicochemical relationships: solubility prediction in organic solvents and water. Nat. Commun. 11, 5753.

Bou-Chacra, N., Melo, K.J.C., Morales, I.A.C., Stippler, E.S., Kesisoglou, F., Yazdanian, M., Löbenberg, R., 2017. Evolution of choice of solubility and dissolution media after two decades of biopharmaceutical classification system. AAPS J. 19, 989–1001.

Brown, C.J., McGlone, T., Yerdelen, S., Srirambhatla, V., Mabbott, F., Gurung, R., Briuglia, M.L., Ahmed, B., Polyzois, H., McGinty, J., Perciballi, F., Fysikopoulos, D., MacFhionnghaile, P., Siddique, H., Raval, V., Harrington, T.S., Vassileiou, A.D., Robertson, M., Prasad, E., Johnston, A., Johnston, B., Nordon, A., Srai, J.S., Halbert, G., ter Horst, J.H., Price, C.J., Rielly, C.D., Sefcik, J., Florence, A.J., 2018. Enabling precision manufacturing of active pharmaceutical ingredients: workflow for seeded cooling continuous crystallisations. Mol. Syst. Des. Eng. 3, 518–549.

Brown, D.G., Wobst, H.J., 2021. A decade of FDA-approved drugs (2010–2019): trends and future directions. J. Med. Chem. 64, 2312–2338.

Butler, J.M., Dressman, J.B., 2010. The Developability Classification System: Application of Biopharmaceutics Concepts to Formulation Development. J. Pharm. Sci. 99, 4940–4954.

Campbell, T.J.S., Rielly, C.D., Benyahia, B., 2022. in *Proceedings of the 32nd European Symposium on Computer Aided Process Engineering*, vol. 51. Elsevier, pp. 775–780.

Cesur, S., Gokbel, S., 2008. Crystallization of mefenamic acid and polymorphs. Cryst. Res. Technol. 43, 720–728.

Chatterjee, S., Moore, C.M.V., Nasr, M.M., 2017. In: Reklaitis, G.V., Seymour, C., García-Munoz, S. (Eds.), Comprehensive Quality by Design for Pharmaceutical Product Development and Manufacture. John Wiley & Sons, Inc, Hoboken, NJ, USA, pp. 9–24.

ChemDecide, Britest, https://www.britest.co.uk/news/archive/britestlaunches_new_decision_software_toolbritest_has_launcheda_suit/, (accessed 27 March 2023).

Chong, M.W.S., McGlone, T., Chai, C.Y., Briggs, N.E.B., Brown, C.J., Perciballi, F., Dunn, J., Parrott, A.J., Dallin, P., Andrews, J., Nordon, A., Florence, A.J., 2022. Temperature correction of spectra to improve solute concentration monitoring by in situ ultraviolet and mid-infrared spectrometries toward isothermal local model performance. Org. Process Res. Dev. 26, 3096–3105.

Cimolai, N., 2014. The potential and promise of mefenamic acid. Expert Rev. Clin. Pharmacol. 289–305.

Cook, J., Cruañes, M.T., Gupta, M., Riley, S., Crison, J., 2014. Quality-by-design: are we there yet? AAPS PharmSciTech 15, 140–148.

De, B.G., 2023. The pharmaceutical industry in 2022: an analysis of FDA drug approvals from the perspective of molecules. Molecules 28, 1038.

Destro, F., Barolo, M., 2022. A review on the modernization of pharmaceutical development and manufacturing – trends,

perspectives, and the role of mathematical modeling. Int. J. Pharm. 620, 121715.

Destro, F., Nagy, Z.K., Barolo, M., 2022. A benchmark simulator for quality-by-design and quality-by-control studies in continuous pharmaceutical manufacturing - intensified filtration-drying of crystallization slurries. Comput. Chem. Eng. 163, 107809.

European Medicines Agency Approach to Facilitating Innovative Manufacturing Approaches, https://ispe.org/pharmaceutical-engineering/ispeak/european-medicines-agency-approach-facilitating-innovative, (accessed 20 February 2023).

Evans, T.W., Sarofim, A.F., Margolis, G., 1974. Models of secondary nucleation attributable to crystal-crystallizer and crystal-crystal collisions. AIChE J. 20, 959–966.

Ferreira, C., Cardona, J., Agimelen, O., Tachtatzis, C., Andonovic, I., Sefcik, J., Chen, Y.C., 2020. Quantification of particle size and concentration using in-line techniques and multivariate analysis. Powder Technol. 376, 1–11.

Z. Frias, P. Arlett and H. Hamann, EMA Strategy on Digitalisation, 2021.

J. Harris and Johnson Matthey, Crystallisation Process Development: White Paper, https://matthey.com/documents/161599/177860/JM-Crystallisation-process-development-whitepaper-digital.pdf/39973c7f-f1a9-f1b7-01d7-b83e6c0bb572?t=1650969179335, (accessed 21 February 2023).

R.E. Hodgett, PhD Thesis, Newcastle University, 2013.

ter Horst, J.P., Turimella, S.L., Metsers, F., Zwiers, A., 2021. Implementation of Quality by Design (QbD) Principles in Regulatory Dossiers of Medicinal Products in the European Union (EU) Between 2014 and 2019. Ther. Innov. Regul. Sci. 55, 583–590.

Hounslow, M.J., Mumtaz, H.S., Collier, A.P., Barrick, J.P., Bramley, A.S., 2001. A micro-mechanical model for the rate of aggregation during precipitation from solution. Chem. Eng. Sci. 56, 2543–2552.

Huhtanen, M., Salmimies, R., Kinnarinen, T., Häkkinen, A., Ekberg, B., Kallas, J., 2012. Empirical modelling of cake washing in a pressure filter. Sep. Sci. Technol. 47, 1102–1112.

ICH Q10 Guideline: Pharmaceutical Quality System, 2008.

ICH Q8(R2) Guideline: Pharmaceutical Development, 2009.

ICH Q3C(R5) Impurities: Guideline for Residual solvents, European Medicines Agency, 2011.

Innovate UK KTN in collaboration with the Advanced Manufacturing Research Centre, Workshop to Explore Accelerated Adoption of Automation and Digitialisation within Medicines Manufacturing, 2022.

ISO 9276–2, https://www.iso.org/standard/57641.html, (accessed 24 May 2023).

Johnson, M.D., Burcham, C.L., May, S.A., Calvin, J.R., McClary Groh, J., Myers, S.S., Webster, L.P., Roberts, J.C., Reddy, V.R., Luciani, C.V., Corrigan, A.P., Spencer, R.D., Moylan, R., Boyse, R., Murphy, J.D., Stout, J.R., 2021. API continuous cooling and antisolvent crystallization for kinetic impurity rejection in cGMP manufacturing. Org. Process Res. Dev. 25, 1284–1351.

Johnson & Johnson Statement on U.S. COVID-19 Vaccine Manufacturing | Johnson & Johnson, https://www.jnj.com/johnson-johnson-statement-on-u-s-covid-19-vaccine-manufacturing, (accessed 17 January 2023).

Karabelas, A.J., 1976. Particle attrition in shear flow of concentrated slurries. AIChE J. 22, 765–771.

Khadra, I., Zhou, Z., Dunn, C., Wilson, C.G., Halbert, G., 2015. Statistical investigation of simulated intestinal fluid composition on the equilibrium solubility of biopharmaceutics classification system class II drugs. Eur. J. Pharm. Sci. 67, 65–75.

Liu, J., Benyahia, B., 2021. Systematic model-based dynamic optimization of a combined cooling and antisolvent multistage continuous crystallization process. Comput. Aided Chem. Eng. 50, 1221–1227.

Lovette, M.A., Albrecht, J., Ananthula, R.S., Ricci, F., Sangodkar, R., Shah, M.S., Tomasi, S., 2022. Evaluation of predictive solubility models in pharmaceutical process development — an enabling

technologies consortium collaboration. Cryst. Growth Des. 22, 5239–5263.

Maloney, A.J., Içten, E., Capellades, G., Beaver, M.G., Zhu, X., Graham, L.R., Brown, D.B., Griffin, D.J., Sangodkar, R., Allian, A., Huggins, S., Hart, R., Rolandi, P., Walker, S.D., Braatz, R.D., 2020. A virtual plant for integrated continuous manufacturing of a carfilzomib drug substance intermediate, part 3: manganese-catalyzed asymmetric epoxidation, crystallization, and filtration. Org. Process Res. Dev. 24, 1891–1908.

Mascia, S., Heider, P.L., Zhang, H., Lakerveld, R., Benyahia, B., Barton, P.I., Braatz, R.D., Cooney, C.L., Evans, J.M.B., Jamison, T.F., Jensen, K.F., Myerson, A.S., Trout, B.L., 2013. End-to-end continuous manufacturing of pharmaceuticals: integrated synthesis, purification, and final dosage formation. Angew. Chem. Int. Ed. 52, 12359–12363.

McGinty, J., Yazdanpanah, N., Price, C., ter Horst, J., Sefcik, J., 2020. *he Handbook of Continuous Crystallisation*. Royal Society of Chemistry.

Mefenamic Acid Specification, https://www.pharmacopoeia.com/bp-2022/monographs/mefenamic-acid.html, (accessed 24 February 2023).

Meng, W., Sirota, E., Feng, H., McMullen, J.P., Codan, L., Cote, A.S., 2020. Effective control of crystal size via an integrated crystallization, wet milling, and annealing recirculation system. Org. Process Res. Dev. 24, 2639–2650.

M. Moorcroft, J. van Kley and B. Sandberg, Small Molecule API Volumes – Trends from the last 15 years of NCEs, https://www.cambrex.com/wp-content/uploads/100791_webinar.pdf (accessed 25 May 2023).

E. Ojo, H. Siddique, I. Houson, R. O'Meadhra, A. Anwar, B. Schenkel and A.J. Florence, in AIChE Annual Meeting 2019, 2019.

ORA Laboratory Manual Volume II: Methods, Method Verification and Validation, Food and Drug Administration: Office of Regulatory Affairs, 2020.

Ottoboni, S., Shahid, M., Steven, C., Coleman, S., Meehan, E., Barton, A., Firth, P., Sutherland, R., Price, C.J., 2020. Developing a batch isolation procedure and running it in an automated semicontinuous unit: AWL CFD25 case study. Org. Process Res. Dev. 24, 520–539.

Ottoboni, S., Wareham, B., Vassileiou, A., Robertson, M., Brown, C.J., Johnston, B., Price, C.J., 2021. A novel integrated workflow for isolation solvent selection using prediction and modeling. Org. Process Res. Dev. 25, 1143–1159.

Ottoboni, S., Brown, C.J., Mehta, B., Jimeno, G., Mitchell, N.A., Sefcik, J., Price, C.J., 2022. Digital design of filtration and washing of active pharmaceutical ingredients via mechanistic modeling. Org. Process Res. Dev. 26, 3236–3253.

Pérez-Calvo, J.-F., Kadam, S.S., Kramer, H.J.M., 2016. Determination of kinetics in batch cooling crystallization processes-a sequential parameter estimation approach. AIChE J. 62, 3992–4012.

Perlmutter, B.A. (Ed.), 2015. in *Practical Guides in Chemical Engineering*. Butterworth-Heinemann, Boston, pp. i–iii.

Pitt, K., Mitchell, G.P., Ray, A., Heywood, B.R., Hounslow, M.J., 2012. Micro-mechanical model of calcium oxalate monohydrate aggregation in supersaturated solutions: effect of crystal form and seed concentration. J. Cryst. Growth 361, 176–188.

Romero, S., 1999. Solubility behavior of polymorphs I and II of mefenamic acid in solvent mixtures. Int. J. Pharm. 178, 193–202.

Rosenberger, J., Butler, J., Dressman, J., 2018. A refined developability classification system. J. Pharm. Sci. 107, 2020–2032.

Sambiagio, C., Marsden, S.P., Blacker, A.J., McGowan, P.C., 2014. Copper catalysed Ullmann type chemistry: from mechanistic aspects to modern development. Chem. Soc. Rev. 43, 3525–3550.

SeethaLekshmi, S., Guru Row, T.N., 2012. Conformational polymorphism in a non-steroidal anti-inflammatory drug, mefenamic acid. Cryst. Growth Des. 12, 4283–4289.

Shahid, M., Sanxaridou, G., Ottoboni, S., Lue, L., Price, C., 2021. Exploring the role of anti-solvent effects during washing on

active pharmaceutical ingredient purity. Org. Process Res. Dev. 25, 969–981.

Sharma, A., Gogate, P.R., 2020. Improvements in crystallization of mefenamic acid using ultrasonic bath operating at two frequencies. Chem. Eng. Process. - Process. Intensif. 147, 107768.

Snapdragon Chemistry Inc. (Boston, MA, United States).

Suresh, P., Basu, P.K., 2008. Improving pharmaceutical product development and manufacturing: impact on cost of drug development and cost of goods sold of pharmaceuticals. J. Pharm. Innov. 3, 175–187.

Szilagyi, B., Nagy, Z.K., 2019. Model-based analysis and quality-by-design framework for high aspect ratio crystals in crystallizer-wet mill systems using GPU acceleration enabled optimization. Comput. Chem. Eng. 126, 421–433.

Szilágyi, B., Eren, A., Quon, J.L., Papageorgiou, C.D., Nagy, Z.K., 2022. Digital design of the crystallization of an active pharmaceutical ingredient using a population balance model with a novel size dependent growth rate expression. From development of a digital twin to in silico optimization and experimental validation. Cryst. Growth Des. 22, 497–512.

TenHoor, C.N., Bakatselou, V., Dressman, J., 1991. Solubility of mefenamic acid under simulated fed- and fasted-state conditions. Pharm. Res 8, 1203–1205.

This value is in the range of compressibility index values characteristics of partially compressible cakes. Cakes formed with organic particles show a partially compressible/compressible behaviour. 2023.

This work was carried out at separate research sites, and whilst ideally product from the wet-milling process development would be used for this parameter estimation, material was unavailable and was therefore generated in situ.

Tien, C., 2012. Principles of Filtration, first ed. Elsevier.

S.J. Urwin, T. Valliant, M.W.S. Chong, A. Nordon and J.H. ter Horst, Consideration of Impurities During Active Crystallization Development: A Case Study with Mefenamic Acid, Prep.

van de Berg, D., Kis, Z., Behmer, C.F., Samnuan, K., Blakney, A.K., Kontoravdi, C., Shattock, R., Shah, N., 2021. Quality by design modelling to support rapid RNA vaccine production against emerging infectious diseases. npj Vaccin. 6, 65.

Vasconcelos, T., Sarmento, B., Costa, P., 2007. Solid dispersions as strategy to improve oral bioavailability of poor water soluble drugs. Drug Discov. Today 12, 1068–1075.

Vassileiou, A.D., Robertson, M., Wareham, B.G., Soundaranathan, M., Ottoboni, S., 2023. A unified AI framework for solubility prediction across organic solvents. Digit. Discov. 2, 356–367.

Vermeire, F.H., Chung, Y., Green, W.H., 2022. Predicting solubility limits of organic solutes for a wide range of solvents and temperatures. J. Am. Chem. Soc. 144, 10785–10797.

Vetter, T., Burcham, C.L., Doherty, M.F., 2014. Regions of attainable particle sizes in continuous and batch crystallization processes. Chem. Eng. Sci. 106, 167–180.

Wakeman, R.J., 1979. Low-pressure dewatering kinetics of incompressible filter cakes, II. Constant total pressure loss or high-capacity systems. Int J. Min. Process 395–405.

Wakeman, R.J., 1979. Low-pressure dewatering kinetics of incompressible filter cakes, I. Variable total pressure loss or low-capacity systems. Int J. Min. Process 5, 379–393.

Wohlgemuth, K., Schembecker, G., 2013. Modeling induced nucleation processes during batch cooling crystallization: a sequential parameter determination procedure. Comput. Chem. Eng. 52, 216–229.

Yu, A.B., Zou, R.P., Standish, N., 1996. Modifying the linear packing model for predicting the porosity of nonspherical particle mixtures. Ind. Eng. Chem. Res. 35, 3730–3741.

Yu, L.X., Amidon, G., Khan, M.A., Hoag, S.W., Polli, J., Raju, G.K., Woodcock, J., 2014. Understanding pharmaceutical quality by design. AAPS J. 16, 771–783.

Zhang, D., Xu, S., Du, S., Wang, J., Gong, J., 2017. Progress of pharmaceutical continuous crystallization. Eng 3 354–3s64.